JGR Atmospheres

RESEARCH ARTICLE
10.1029/2021JD034882

Practical and Intrinsic Predictability of Wave-Convection Coupled Bands Over Southern China

Yu Du[1,2,3], Fuqing Zhang[4], Y. Qiang Sun[5], Junhong Wei[1,2,3], and Xiaoqing Li[1]

[1]School of Atmospheric Sciences, Sun Yat-sen University, and Southern Marine Science and Engineering Guangdong Laboratory (Zhuhai), Zhuhai, China, [2]Guangdong Province Key Laboratory for Climate Change and Natural Disaster Studies, Sun Yat-sen University, Zhuhai, China, [3]Key Laboratory of Tropical Atmosphere-Ocean System (Sun Yat-sen University), Ministry of Education, Zhuhai, China, [4]Department of Meteorology and Atmospheric Science, Center for Advanced Data Assimilation and Predictability Techniques, The Pennsylvania State University, University Park, PA, USA, [5]Cooperative Institute for Modeling the Earth System, Program in Oceanic and Atmospheric Sciences, Princeton University, Princeton, NJ, USA

Key Points:

- Almost all 20 ensemble members can capture the wavelike pattern of convective bands but with varying wave features
- The practical predictability depends on the correct thermodynamical initial state, and to a lesser degree on physical parameterizations
- The wavelike pattern of bands is generally predictable but the exact location of each band has an intrinsic predictability barrier

Supporting Information:

Supporting Information may be found in the online version of this article.

Correspondence to:

Y. Du,
duyu7@mail.sysu.edu.cn

Citation:

Du, Y., Zhang, F., Sun, Y. Q., Wei, J., & Li, X. (2021). Practical and intrinsic predictability of wave-convection coupled bands over southern China. *Journal of Geophysical Research: Atmospheres*, *126*, e2021JD034882. https://doi.org/10.1029/2021JD034882

Received 10 MAR 2021
Accepted 21 OCT 2021

Abstract The practical and intrinsic predictability of wave-convection coupled bands that occurred near the south coast of China on January 30, 2018 lasting nearly 10 hr are investigated through convection-permitting ensembles and relevant sensitivity experiments. Although almost all 20-member ensembles can capture the wavelike pattern of convective bands, their wavelength and period vary among the ensembles. The GOOD and POOR runs are further conducted and initialized using the composite of initial conditions from good and poor members selected based on the performance of the simulated wave characteristics. Both the GOOD and POOR runs exhibit wave ducting structures for gravity waves, but the GOOD run tends to have higher precipitable water over the land, which results in a more evident wave pattern of convective bands on land in the GOOD run. Their differences in precipitable water are mainly attributed to the differences in the initial conditions of humidity and temperature at low-middle levels. The practical predictability depends on the correct initial state in terms of thermodynamics, and to a lesser degree on physical parameterizations. To further explore their intrinsic predictability, a series of sensitivity experiments were performed with the linear weighted initial conditions from the GOOD and POOR runs. The pattern of wave-convection coupled bands is generally predictable (forecast lead time <~12 hr) but their phase (the exact location of each band) has an intrinsic predictability barrier even with minute initial perturbations due to the rapid small-scale error growth associated with gravity waves and moist convection.

1. Introduction

Mesoscale wavelike convection bands are often observed by radars or satellites around the globe, such as "morning glory cloud" in Australia (Clarke, 1972) and cloud bands in the snow bomb event of northeastern United States (Bosart et al., 1998). Since the wavelike convection bands are always coupled and interacted synergistically with mesoscale gravity waves (Cram et al., 1992; Miller & Sanders, 1980; Ruppert & Bosart, 2014; Uccellini & Koch, 1987; Zhang et al., 2001), we thus called them "wave-convection coupled bands."

Two main mechanisms have been proposed to explain this unique phenomenon "wave-convection coupled bands": wave-CISK (wave-convection interaction) theory and wave ducting theory. The wave-convection interaction theory describes positive feedback processes between convection and gravity waves, where convection provides energy to gravity waves by latent heating whereas gravity waves in turn initiate and organize convection (Koch et al., 1988; Lane & Zhang, 2011; Lindzen, 1974; Raymond, 1984, 1987). On the other hand, in the wave ducting theory, gravity waves can propagate horizontally in a wave duct that maintains gravity waves near the surface for a long duration and holds the energy of gravity wave in the low troposphere (Bosart et al., 1998; Lindzen & Tung, 1976; Powers & Reed, 1993; Zhang & Koch, 2000), which provides a favorable condition for wave-convection coupling in the low troposphere.

On January 30, 2018, a banded convective event occurred near the south coast of China lasting a long time (~10 h) with periodic moderate rainfall, which was found to be associated with mesoscale gravity waves with a wave speed of ~12 m s^{-1} and a primary wavelength of about ~40–50 km (Du & Zhang, 2019, hereafter DZ19). Convection-allowing simulations can generally reproduce the wave-convection coupled bands, and

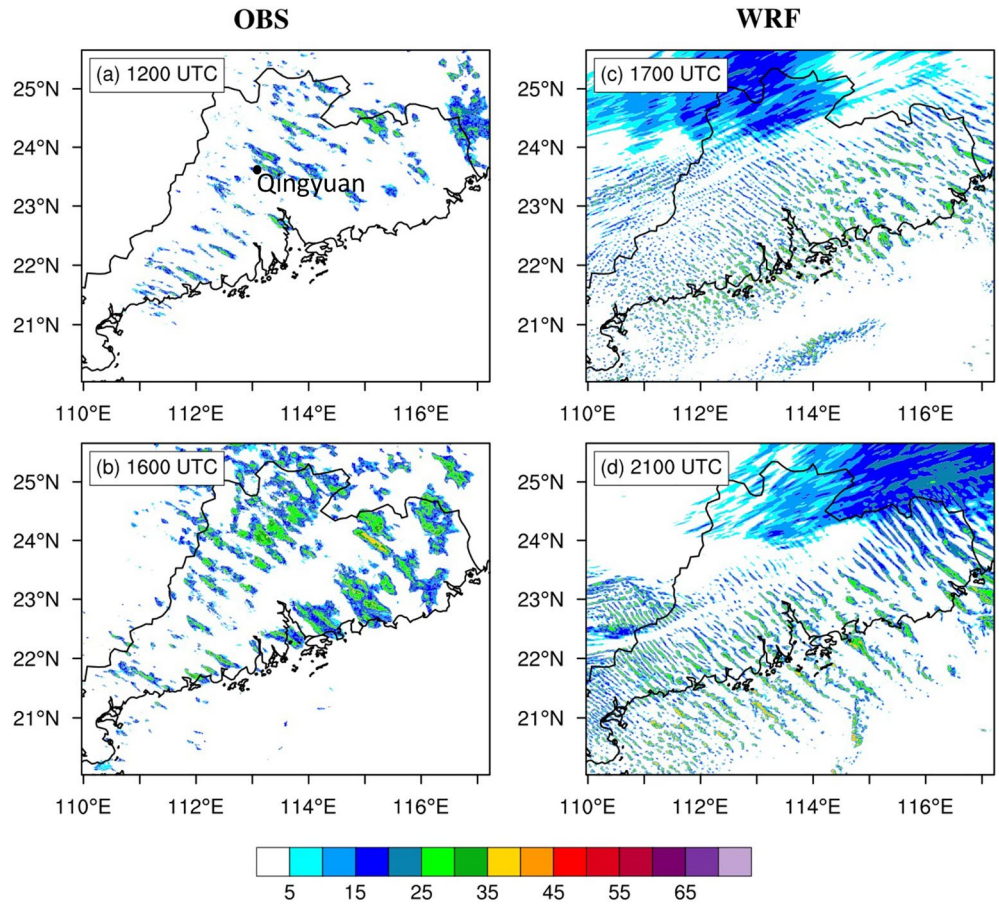

Figure 1. Observed radar reflectivity (dBZ) at 2,500 m at (a) 12:00 UTC and (b) 16:00 UTC January 30, 2018. Simulated radar reflectivity at 2,500 m (c) 17:00 UTC and (d) 21:00 UTC January 30, 2018. A black dot in (a) indicates Qingyuan station.

reveal that both wave ducting and wave-convection interaction exert a combined effect on the bands. The wave ducting in the present case is characterized by a thick low-level stable layer capped by a low-stability reflecting layer with a critical level and small Richardson number surrounding, which is consistent with the theory of Lindzen and Tung (1976). The convective bands propagate coordinately with peak updraft regions of gravity waves, indicating that strong interactions of convection and gravity waves. Although we have already presented the dominant maintenance mechanisms of this coherence phenomenon, its prediction using numerical models is less discussed. Compared to large-scale systems or mesoscale convective systems (Melhauser & Zhang, 2012), very little is known about the predictability of the wave-convection coupled bands. Understanding the sources of forecasting uncertainties and error growth dynamics in the numerical weather prediction of the wave-convection coupled bands is important in predicting this phenomenon.

Atmospheric predictability refers to the sensitivity to initial conditions and model errors in numerical weather prediction models, which is studied starting with Thompson (1957) and Lorenz (1963, 1969). Anthes et al. (1985) began to investigate the mesoscale predictability. The errors of mesoscale weather systems associated with convection and moist processes grow rapidly due to nonlinear effects (Crook, 1996; Gilmore & Wicker, 1998; Hohenegger & Schar, 2007; Park, 1999). The error growth is particularly sensitive to the initial fields of moisture and temperature (Park & Droegemeier, 2000). Therefore, the predictability of mesoscale weather systems can be intrinsically limited by the moisture processes (Bei & Zhang, 2007; Tan et al., 2004; Zhang et al., 2003, 2007, 2016).

Atmospheric predictability can be categorized into two types (Lorenz, 1996; Melhauser & Zhang, 2012; Sun & Zhang, 2016; Ying & Zhang, 2017; Zhang et al., 2019): (a) practical predictability that refers to the ability

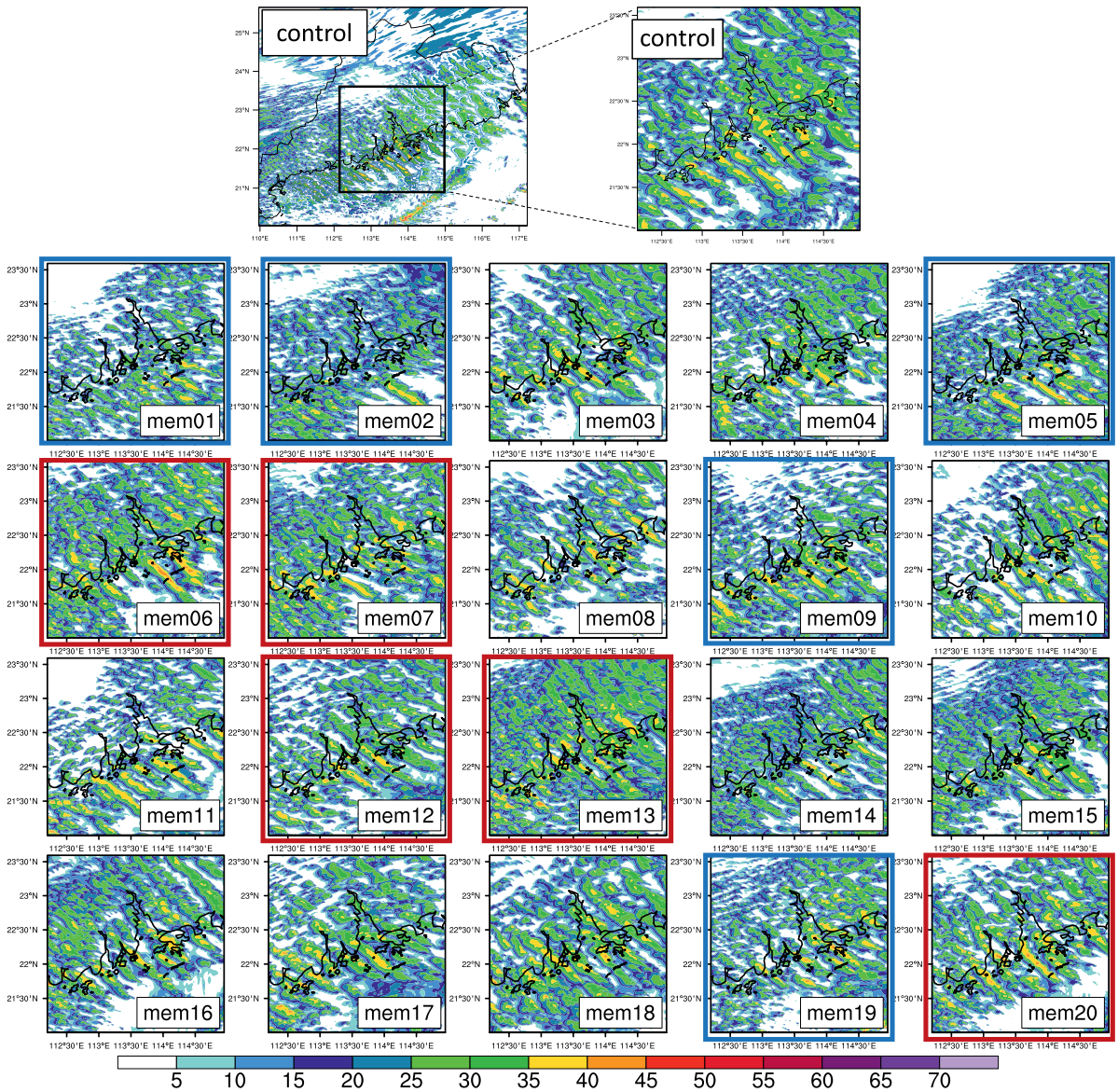

Figure 2. A mosaic of 20 ensemble members depicting simulated radar composite reflectivity at 19:00 UTC January 30, 2018 compared with the control run. The red and blue frames indicate good and bad members, respectively.

to predict based on the currently available conditions, and is limited by uncertainties in the prediction model and initial conditions, and (b) intrinsic predictability that refers to the ability to predict given a nearly perfect forecast model with nearly perfect initial conditions. The practical predictability limit can be extended as errors in the model or the initial conditions decrease, whereas the intrinsic predictability limit will not change even if the initial errors are further reduced. The uncertainties in terms of practical predictability remain sizeable and are limited by the current capability of observations, modeling, and data assimilation. The intrinsic predictably is often examined based on a perfect model assumption made in conjunction with initial condition uncertainties an order of magnitude smaller than the current observational analysis in the previous studies (e.g., Judt, 2018; Mapes et al., 2008; Melhauser & Zhang, 2012; Tribbia & Baumhefner, 2004; Zhang et al., 2003, 2007). To the best of our knowledge, the practical and intrinsic predictability of wave-convection coupled bands are rather underexplored.

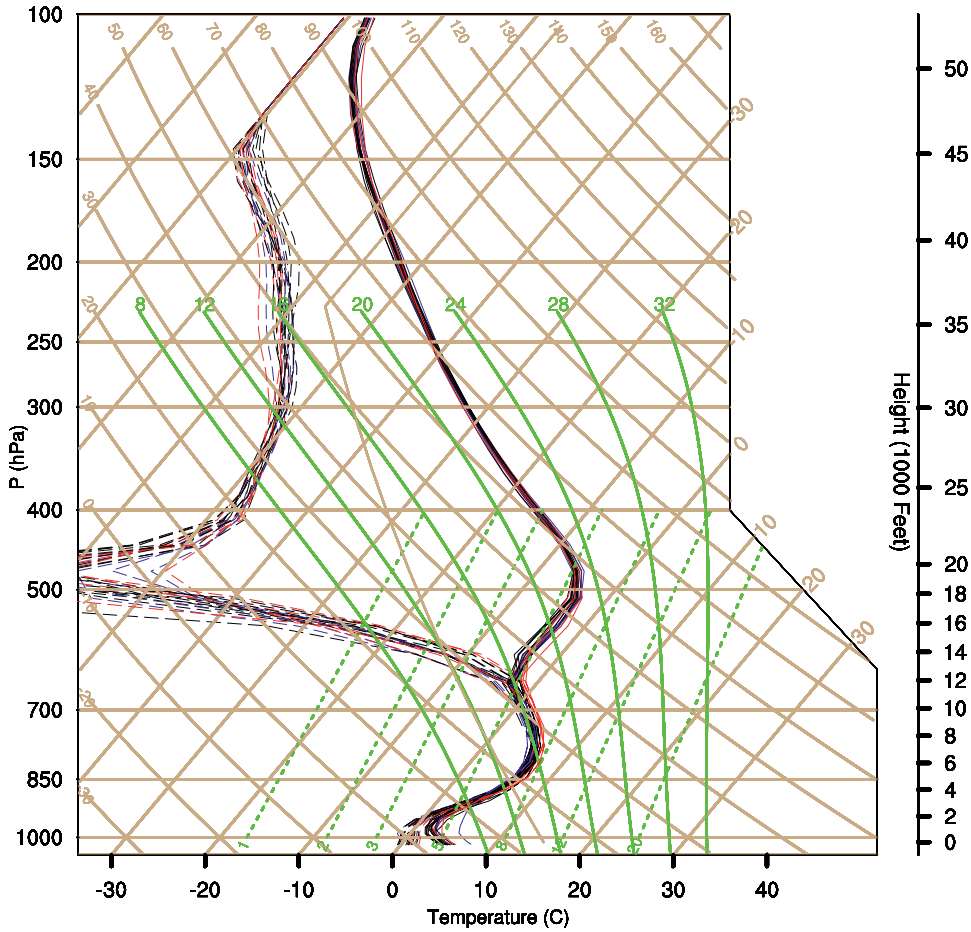

Figure 3. Skew *T*-log *p* diagrams at Qingyuan at 19:00 UTC January 30, 2018 from 20-ensemble members (red: good members; blue: poor members; black: fair members). The location of Qingyuan is indicated in Figure 1a. Solid and dashed lines represent temperature and dew point temperature, respectively.

Therefore, the objective of the present study is to examine the practical and intrinsic predictability of the wave-convection coupled bands in South China at 12:00 UTC January 30, 2018 using a series of convection-permitting ensembles and sensitivity experiments. The rest of the paper is organized as follows. In Section 2, an overview is given for the case of the wave-convection coupled bands, and the results of DZ19 are reviewed. The model configuration and experimental design are described in Section 3. The practical and intrinsic predictability are discussed in Sections 4 and 5, respectively. Finally, concluding remarks can be found in Section 6.

2. Case Overview

At 12:00 UTC January 30, 2018, a southwest-northeast oriented surface cold front approached the south coast of China (Figure 4 of DZ19). At that time, Guangdong Province was located on the cold side of the surface cold front with prevailing northeasterly winds near the surface. Since the cold front system was northward tilted with height, a southwest-northeast oriented shear line at 850 hPa occurred at the north edge of Guangdong Province, where the southerly winds prevailed at 850 hPa. The vertical wind shear was thus pronounced at low levels.

Multiple northwest-southeast oriented convective bands, with the long-dimensional horizontal extent of 100–300 km, occurred over Guangdong (Figures 1a and 1b), and lasted for nearly 10 hr from 08:00 to 18:00 UTC January 30, 2018 (Figure 1 of DZ19). Such convective bands exhibited apparent wave features with their horizontal spacing distance of ~50 km and propagated northeastward at a speed of around 12 m s^{-1}.

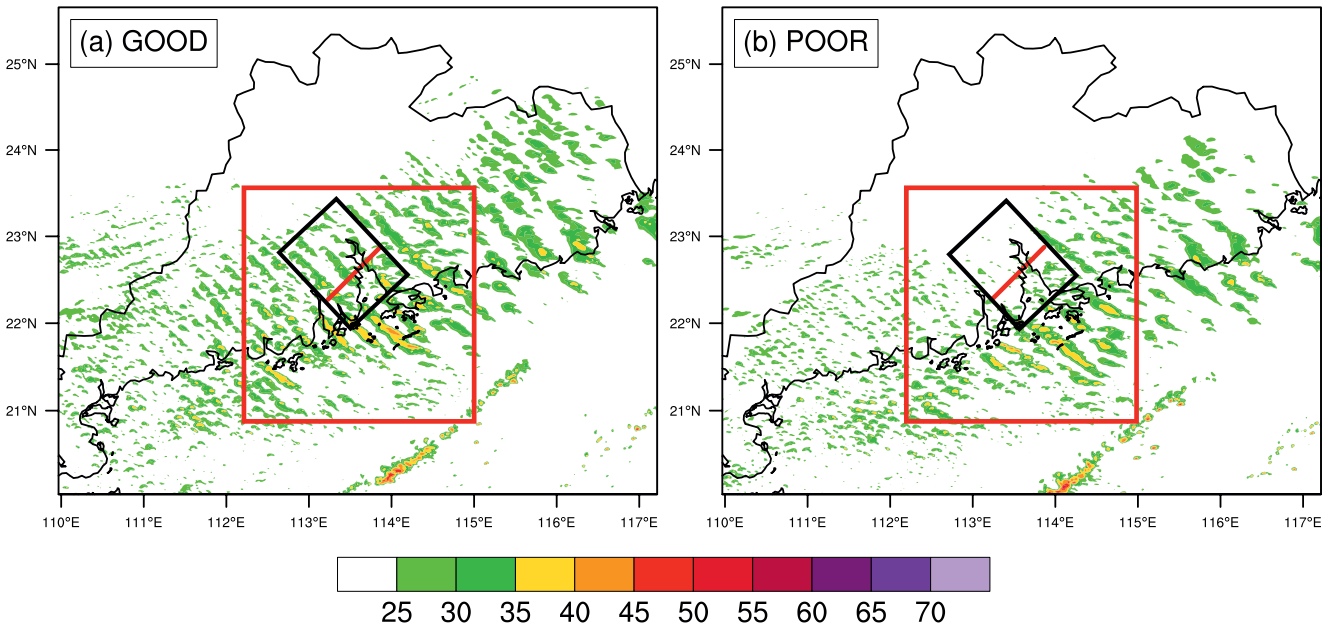

Figure 4. Simulated radar composite reflectivity at 19:00 UTC January 30, 2018 in the (a) GOOD run and (b) POOR run. The red box is used in Figure 10. The black box is used for the calculation of power spectrum in Figure 6. The red line is used for the vertical cross section in Figures 5, 7, and 18.

DZ19 found evidence of a wave duct at low levels that contained a strong stable layer below 850 hPa and was capped by a moist neutral stability layer within 850-600 hPa. A critical level with Richardson number of <0.25 was embedded in the moist neutral stability layer. Such environmental settings kept gravity waves propagating horizontally in the wave duct for a long period of time without losing much energy. According to the theory of wave ducting proposed by Lindzen and Tung (1976), the wave speed is determined by the strength and depth of the low-level stable layer as

$$C = \frac{N_m D}{\pi\left(\frac{1}{2} + n\right)} + U = 12.2 \text{ m/s} \quad (1)$$

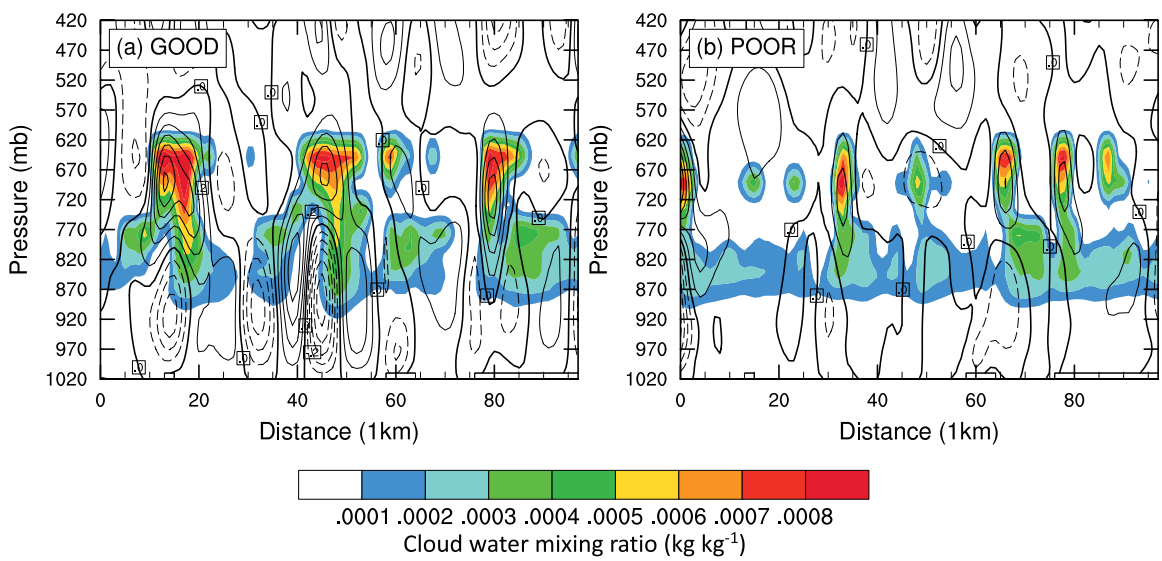

Figure 5. Wave-parallel vertical cross section of cloud water mixing ratio (shading, kg kg^{-1}) and vertical motion (contour, m s^{-1}) compositing (averaging) along the red line of Figure 4 at 19:00 UTC January 30, 2018 in the (a) GOOD run and (b) POOR run. The left (right) side of *x* axis is southwest (northeast) side.

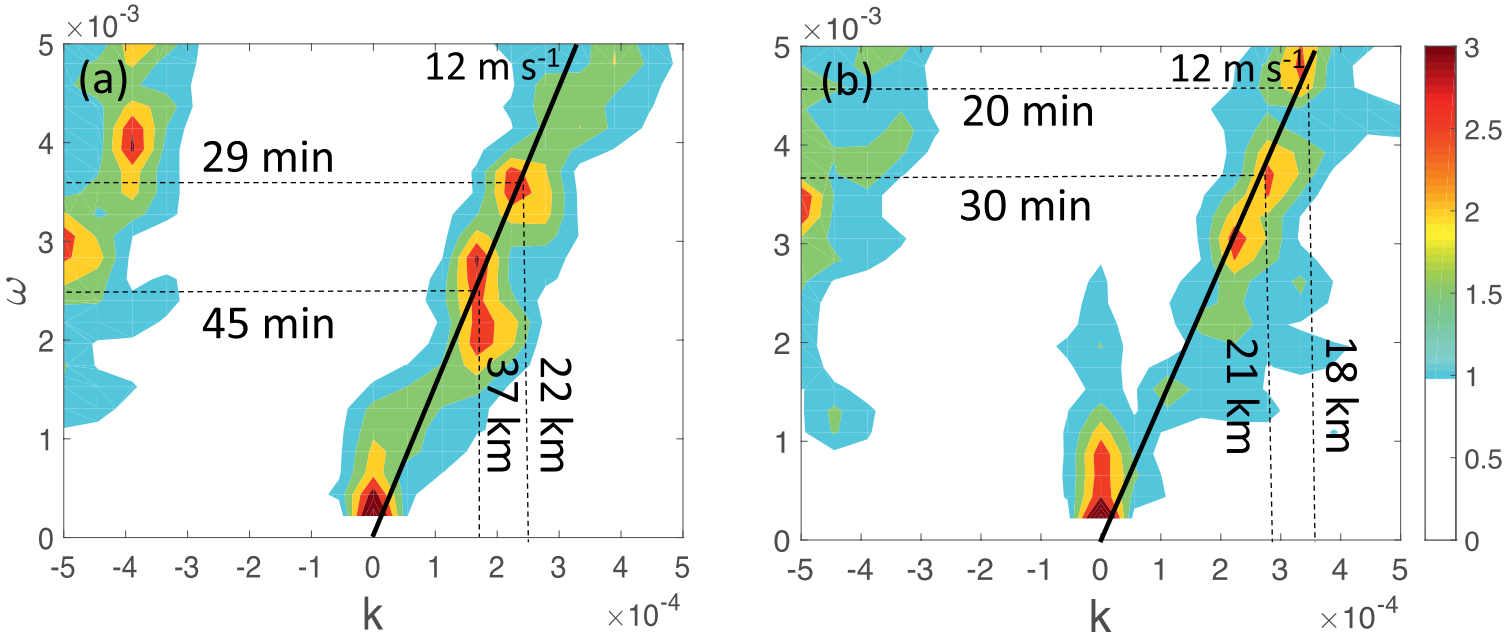

Figure 6. Power spectrum of the 4-km cloud mixing ratio in the black box of Figure 4 divided by a smoothed background spectrum from (a) the GOOD run and (b) the POOR run. The black solid line depicts phase speed ω/k. The black dash lines indicate the horizontal wavelengths and wave periods for the peaks.

where $D = 1.5$ km is the depth of the low-level stable layer, $N_m = 0.016$ s^{-1} is moist static stability, and $U = -3$ m s^{-1} is the mean background wind in the wave-parallel direction in the stable layer. The propagation speed of convective bands is in agreement with the calculated ground-relative wave speed for the primary mode ($n = 0$) based on the wave ducting theory (Lindzen & Tung, 1976). Besides wave ducting, the latent heating from moist convection in the wave-convection interactions plays a role in the formation and maintenance of gravity waves by providing energy. Sensitivity experiments in DZ19 further verify the coexistence of wave ducting and wave-convection interaction in this case.

3. Model Configuration and Experimental Design

3.1. Model Configuration and Evaluation

In the present study, the Weather Research and Forecasting (WRF Version 3.8.1; Skamarock et al., 2008) model is employed to conduct a control simulation and ensembles. The model configuration is the same as that described in DZ19. One-way nested domains (d01, d02, and d03) with 9-km, 3-km, and 1-km horizontal grid spacing and 51 vertical levels are used. The absorbing layer of gravity waves is introduced at the top of 50 hPa with a layer of 5 km. The Kain-Fritsch convection parameterization (Kain, 2004) is used in d01 but turned off in d02 and d03. All domains use the Thompson et al. (2008) microphysics scheme, the YSU boundary-layer scheme (Hong et al., 2006), the Rapid Radiative Transfer Model for Global Climate Models (RRTMG) longwave-radiation and shortwave-radiation schemes (Iacono et al., 2008), the revised MM5 Monin-Obukhov surface-layer scheme (Jiménez et al., 2012), and the unified Noah land surface model (Livneh et al., 2011). The control simulation is initialized at 12:00 UTC January 30, 2018 by the first member of the Global Ensemble Forecast System (GEFS) (Toth & Kalnay, 1993). The GEFS conducted by NCEP is a weather forecast model including 21 ensemble members.

The wave-convection coupled bands in the control run (Figures 1c and 1d) are generally similar to those in the simulation of DZ19 that was initiated by NCEP FNL (final) operational global analysis data. As shown in Figures 1c and 1d, the control run can simulate the northwest-to-southeast oriented wavelike convective bands over Guangdong as observations. Compared to observations, the simulated wavelike convective bands show a similar propagation speed of 11.5 m/s, a similar lasting long period of nearly 10 hr, and similar amplitudes of wavelike bands (~35 dBZ). The simulated wavelength of bands ranges within tens of kilome-

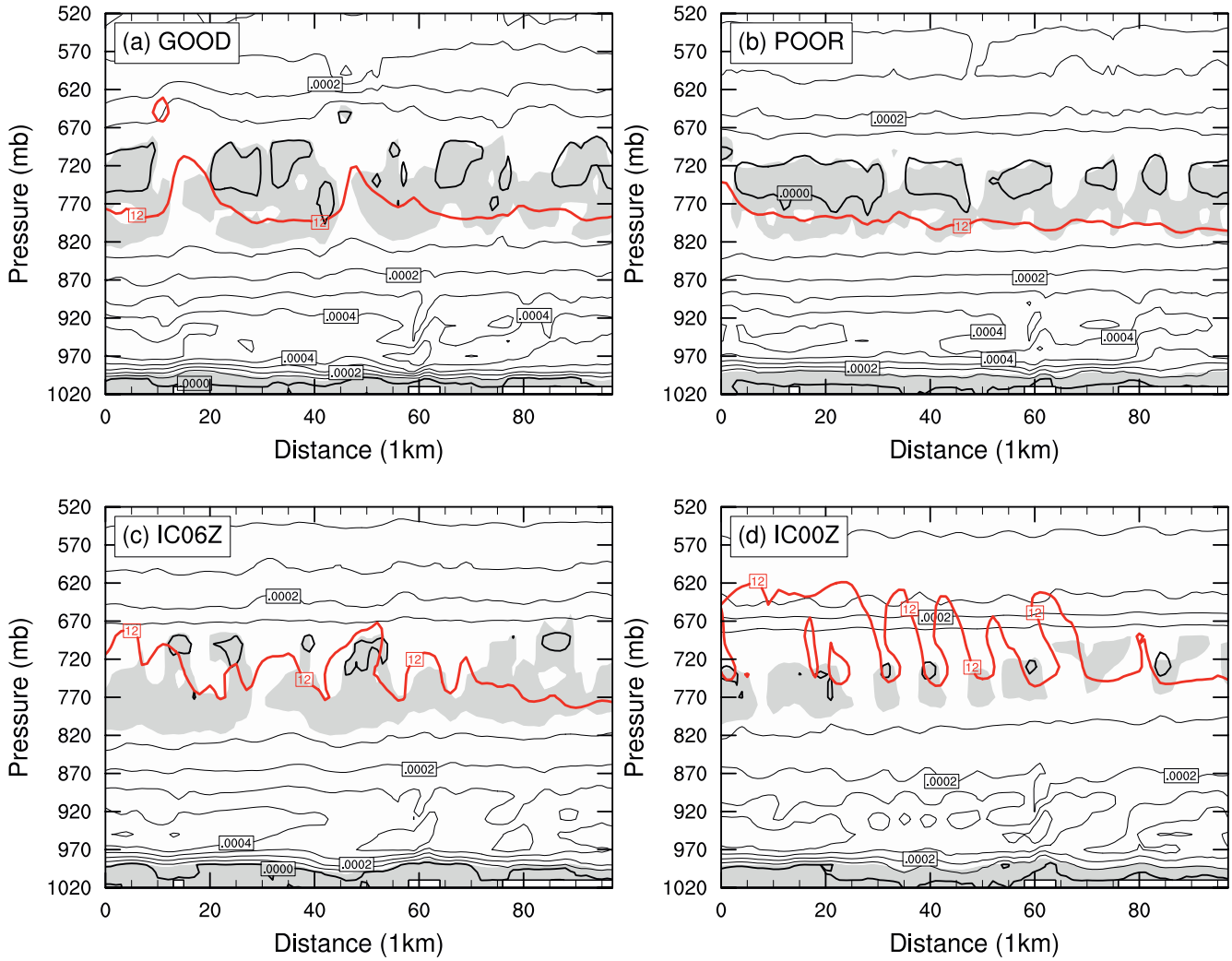

Figure 7. Wave-parallel vertical cross section of square of moist Brunt-Väisälä frequency (s^{-2}, contour) in the (a) GOOD, (b) POOR, (c) IC06Z, and (d) IC00Z runs. The gray shading indicates Richardson number Ri < 0.25 and the red line shows the critical level, assuming a wave speed of 12 m s^{-1}.

ters as the observations but with a smaller primary horizontal wavelength of ~20–40 km. The occurrence of the simulated wave pattern is delayed by a few hours (~5 hr) and its exact location tends to be more to the south (ocean side). Generally, the simulation can capture the wavelike pattern of convective bands.

3.2. Experimental Design

To study the practical and intrinsic predictability of the wave-convection coupled bands, we conducted a series of 20-member ensembles initialized with the 2nd–21st members of GEFS. A mosaic of 20 ensemble members depicting simulated radar composite reflectivity at 19:00 UTC is shown in Figure 2. The ensemble set has similar wavelike features as well as provides a wide variety of forecasts in terms of many important aspects of the wave characteristics, highlighting the limit of practical predictability because of the relatively large ensemble spread. Some members produce evident wavelike bands over Guangdong (e.g., mem06), whereas in some members convective bands are relatively weak over the land and/or do not exhibit pronounced wavelike features (e.g., mem01). Considering a significant wave pattern with a primary horizontal wavelength of ~50 km in the observations (DZ19), we applied two-dimensional (frequency-wave number) spectrum used in Wheeler and Kiladis (1999) and DZ19 for each ensemble member (Figure S3 in Supporting Information S1). No peak was found near the primary horizontal wavelength of ~30–50 km and the

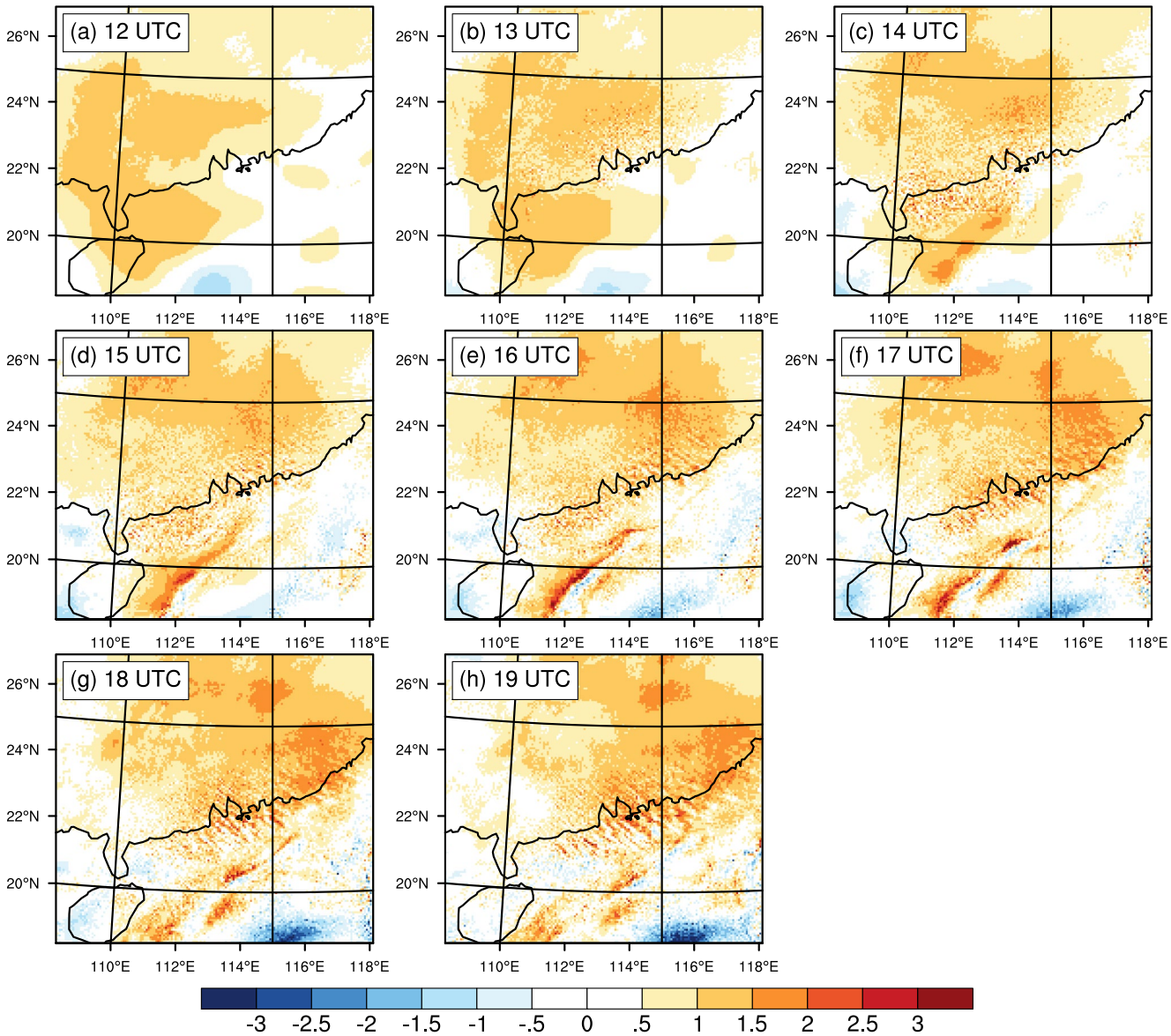

Figure 8. The evolution of the difference of precipitable water (kg m^{-2}) between the GOOD and POOR runs during 12:00–19:00 UTC January 30, 2018.

primary period of 40–70 min in the frequency-wave number spectrum in five ensemble members (mem01, 02, 05, 09, and 19), which are thus selected as poor members. Among the remaining 15 members, we further selected the same number of five members as good member representatives (mem06, 07, 12, 13, and 20) based on the errors of primary and secondary wavelength as well as wavelike patterns of convective bands in Figure 2. Therefore, three groups were selected into good (five members), fair (10 members), and poor (five members) classification. We mainly focus on the five good and five poor representations to identify two distinct modes of wave-convection coupled bands in the present study.

We further performed WRF simulations which are initialized by averaging all prognostic variables (e.g., u, v, T, p, etc.) in the initial conditions of the five good members or five poor members, which are called GOOD run and POOR run, respectively. Through comparison of the GOOD and POOR runs, the key factors affecting forecasts and their main error sources are analyzed. Simulations with different initial time (06:00 UTC January 30 and 00:00 UTC January 30) and physical schemes (MYJ, MYNN PBL schemes; Kessler and Lin microphysics schemes) are also conducted to investigate the practical predictability of bands.

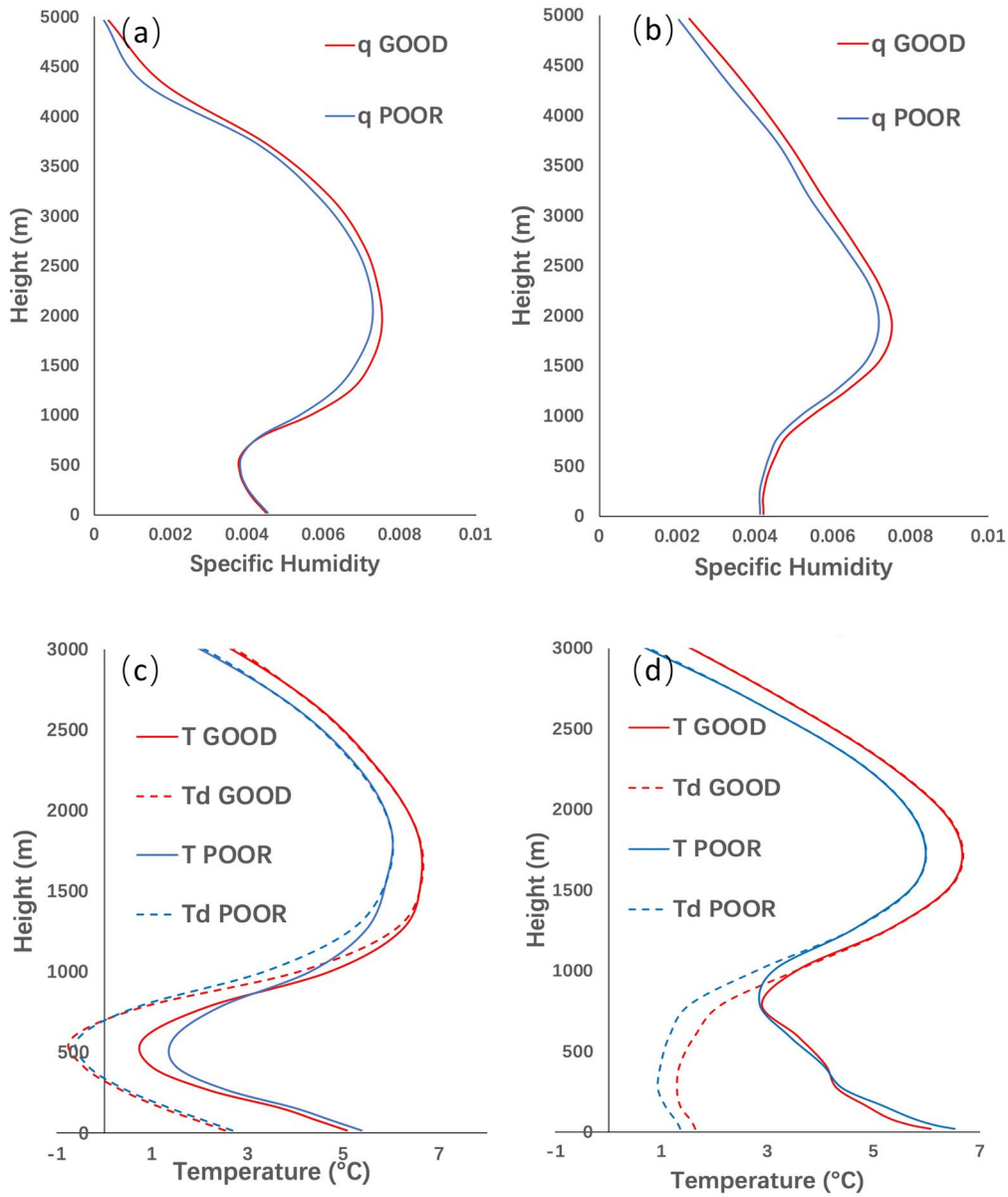

Figure 9. The vertical profile of (a, b) specific humidity (kg kg^{-1}) and (c, d) temperature (solid lines, °C), dew temperature (dashed lines, °C) in the GOOD and POOR runs at Qingyuan at (a, c) 12:00 UTC and (b, d) 19:00 UTC January 30, 2018.

To examine the sensitivity to small uncertainties in the initial conditions and explore the intrinsic predictability limit for this event, nine additional experiments from R1 to R9 are conducted (Melhauser & Zhang, 2012), which are initialized with linearly averaging all prognostic variables in the initial conditions of the GOOD and POOR runs with a specified weight as

$$\mathrm{RX} = \frac{X}{10}\mathrm{GOOD} + \frac{10 - X}{10}\mathrm{POOR} \tag{2}$$

where X is the experiments number 1–9. Therefore, R9 (R1) run is the closest to the GOOD (POOR) run.

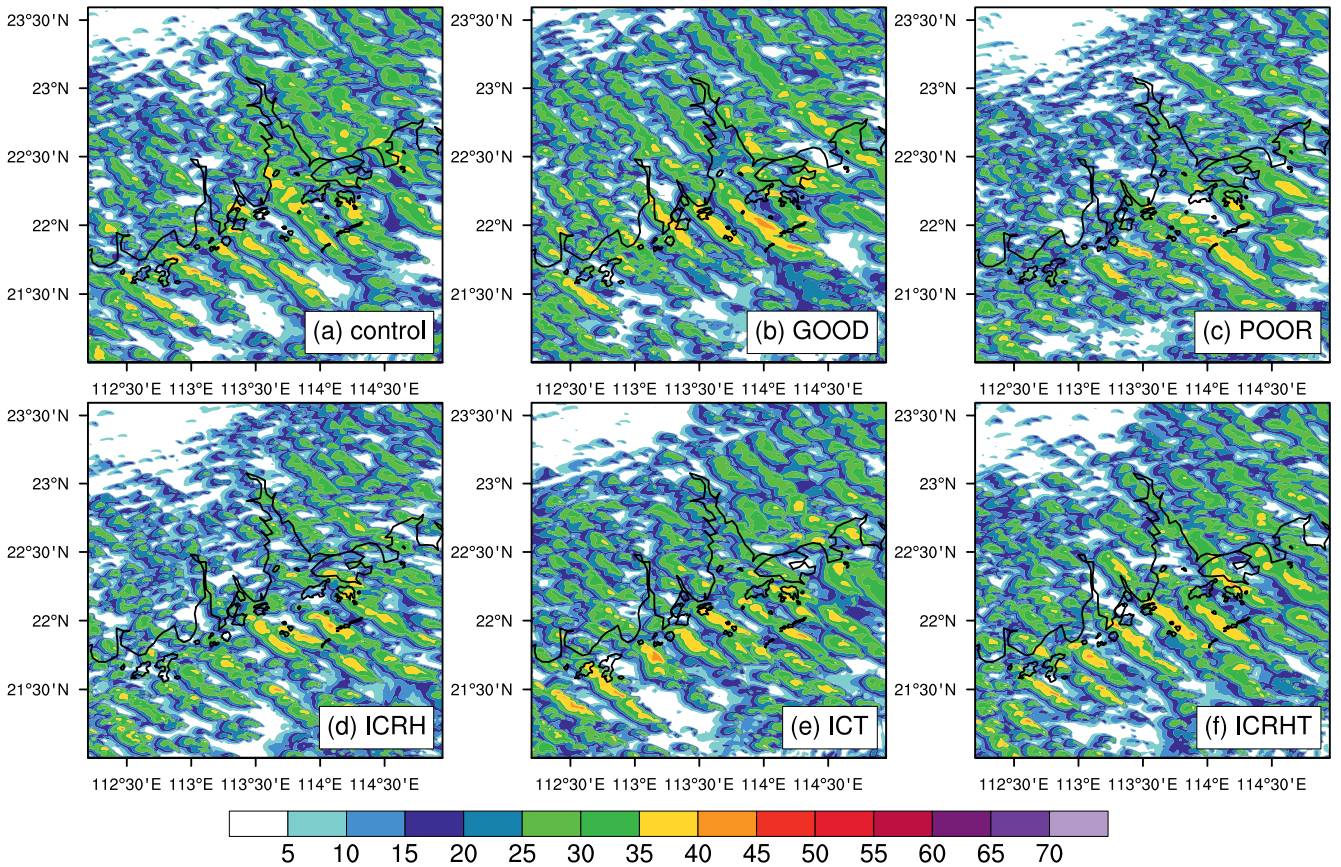

Figure 10. Simulated Radar composite reflectivity in the red box of Figure 4 at 19:00 UTC January 30, 2018 in the (a) control, (b) GOOD, (c) POOR, (d) ICRH, (e) ICT, and (f) ICRHT runs.

4. Practical Predictability

4.1. Sensitivity to Initial Condition Uncertainties From Ensembles

Figure 2 presents the ensemble simulations of the wave-convection coupled bands characterized by large ensemble spread including good (mem06, 07, 12, 13, and 20), fair (mem03, 04, 08, 10, 11, 14, 15, 16, 17, and 18), and poor (mem01, 02, 05, 09, and 19) ensemble members. Good members manifest as evident wavelike northwest-southeast oriented convective bands both over the land and ocean, but poor members show weak convective bands over the land. However, the vertical structures of temperature and moisture are quite similar among those ensemble members (Figure 3). As shown in Figure 3, all ensembles can generally capture such "stable-neutral-stable" sandwich-like stratification, which fundamentally satisfies the theory of Lindzen and Tung (1976). The atmosphere below 600 hPa is nearly saturated, while the layer above 600 hPa is relatively dry. The low-level stable layer below 850 hPa is capped by a nearly neutral moist stability layer within 850–600 hPa as well as the stable layer within 600–500 hPa.

In order to elucidate the differences between good and bad members, we focus on the comparison of the GOOD and POOR runs (Figure 4) which are WRF simulations initialized with composite of GEFS from good and poor members, respectively. As shown in Figure 4, the GOOD run exhibits obvious wavelike features, while the POOR run produces weaker convection over the land though wavelike features are still significant over the ocean. The GOOD (POOR) run can well represent the performance of the good (poor) members. To further illustrate their vertical structures, Figure 5 presents the vertical cross section of cloud water mixing ratio and vertical motion along a red line of Figure 4 from the GOOD and POOR runs. In the cross section of the GOOD run (Figure 5a), three moderately deep convective bands have a spacing distance of around 40 km and extend to the 600-hPa level. The strong upward motion well matches the convective region, whereas small upward motion or downward motion corresponds to the region between convective

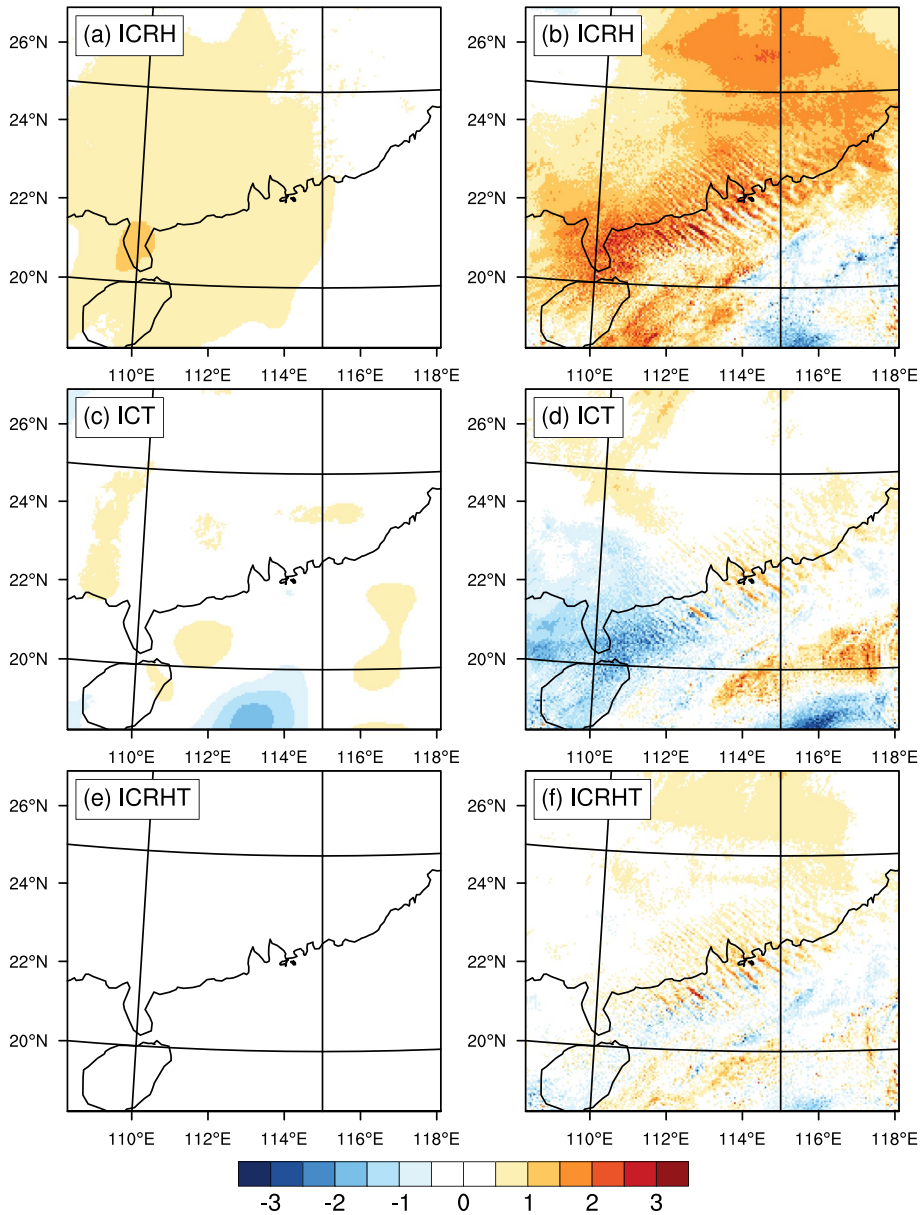

Figure 11. The difference of precipitable water (kg m^{-2}) between the GOOD run and (a and b) ICRH, (c and d) ICT, (e and f) ICRHT runs at (a, c, and e) 12:00 UTC and (b, d, and f) 19:00 UTC January 30, 2018.

bands (Figure 5a). The strong upward motion (maximum convective latent heating) near 670 hPa follows behind the axis of strongest upward motion below 800 hPa (also read Ralph et al., 1993 and Lin, 1987). However, in the POOR run (Figure 5b), convection is relatively weak with a smaller spacing of around 20 km, and the wave feature is not as significant as that in the GOOD run. The upward motion also corresponds to the convective region in the POOR run (Figure 5b).

Following DZ19, two-dimensional (frequency-wave number) power spectrums of the 4-km cloud mixing ratio are performed in the GOOD and POOR runs as shown in Figure 6. The power spectrum is calculated by two overlapping 8-hr time periods (0–8 h, 4–12 hr) with 10-min time resolution and is divided by the smoothed background spectrum to demonstrate the spectrum peaks more clearly (Lane & Zhang, 2011; Wheeler & Kiladis, 1999). In the GOOD run (Figure 6a), two peaks exist in the frequency-wave number space: the primary peak at the horizontal wavelength of ~37 km and the period of ~45 min, and the sec-

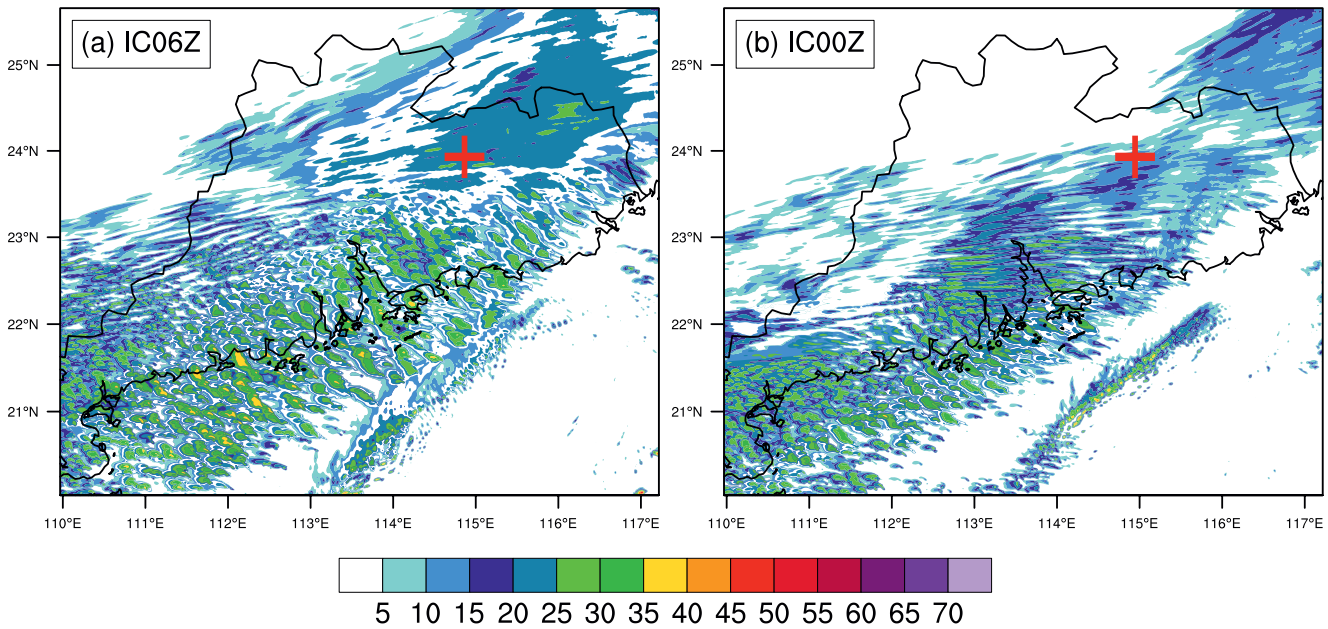

Figure 12. Simulated radar composite reflectivity at 19:00 UTC January 30, 2018 in the (a) IC06Z run and (b) IC00Z run.

ondary peak at the horizontal wavelength of ~22 km and the period of 29 min. Since the wave and convection are found to be coupled (DZ19), the primary and secondary peaks represent the deeper and shallower convection with larger and smaller wavelength (period), respectively. The slope of the line following the peaks (ω / k) shows the phase speed of ~12 m s^{-1}, which indicates the northeastward propagation speed of the banded convection. The wave features shown above are similar to the results in the control run of DZ19. In contrast, peaks in the frequency-wave number space of the POOR run (Figure 6b) exhibit smaller wavelengths (18 and 21 km) and shorter periods (20 and 30 min) compared to the GOOD run. The propagation speed of the wave-convection coupled bands in the POOR run is similar to that in the GOOD run.

To clarify the difference in wave features between the GOOD and POOR runs, we examine the structures of the wave ducting as presented in DZ19 for the GOOD and POOR runs. Figure 7 shows the vertical cross section of the square of moist Brunt-Väisälä frequency (N_m^2) in the two runs. With regard to the calculation of N_m^2, please refer to DZ19. The two runs exhibit similar three-layer stratifications: the low-level stable layer below 850 hPa ($0.0001\ s^{-2} < N_m^2 < 0.0004\ s^{-2}$) is capped by the middle-level (850-650 hPa) less-stable layer ($N_m^2 \sim 0\ s^{-2}$) while the less-stable layer is overlaid by an aloft stable layer ($N_m^2 > 0.0002\ s^{-2}$). In the two runs, the critical level, where the wave phase velocity (~12 m s^{-1}) matches the background wind in the direction of wave direction ($\bar{U}$), is embedded within the middle-level less-stable layer. The local gradient Richardson number ($\mathrm{Ri} = N_m^2 / \left(\frac{\partial \bar{U}}{\partial z}\right)^2$) < 0.25 surrounds the critical level. Therefore, the stratification of both the GOOD and POOR runs matches well the typical wave ducting proposed by Lindzen and Tung (1976).

Since the wave ducting is excluded as the possible cause of the differences in wave features between the GOOD and POOR runs, we further examine their moisture features and processes for the two runs. Figure 8 presents the evolution of the difference of precipitable water between the GOOD and POOR runs during 12:00–19:00 UTC. The precipitable water over Guangdong in the GOOD run is significantly higher than that in the POOR starting from the initial time and retaining its preponderance throughout the whole case period. From the perspective of thermodynamics, the weaker precipitable water in the POOR run is not favorable to the convection, and thus results in relatively weak wave-convection coupled bands in the POOR run compared to the GOOD run. Since the wave and convection are coupled, wave periods are related to the life cycles of convection (DZ19). The horizontal wavelength ($\lambda_x = T\left(c + \bar{U}\right)$) is thus smaller in the POOR run due to a shorter life cycle (T) and a similar relative-ground wave speed ($c + \bar{U}$).

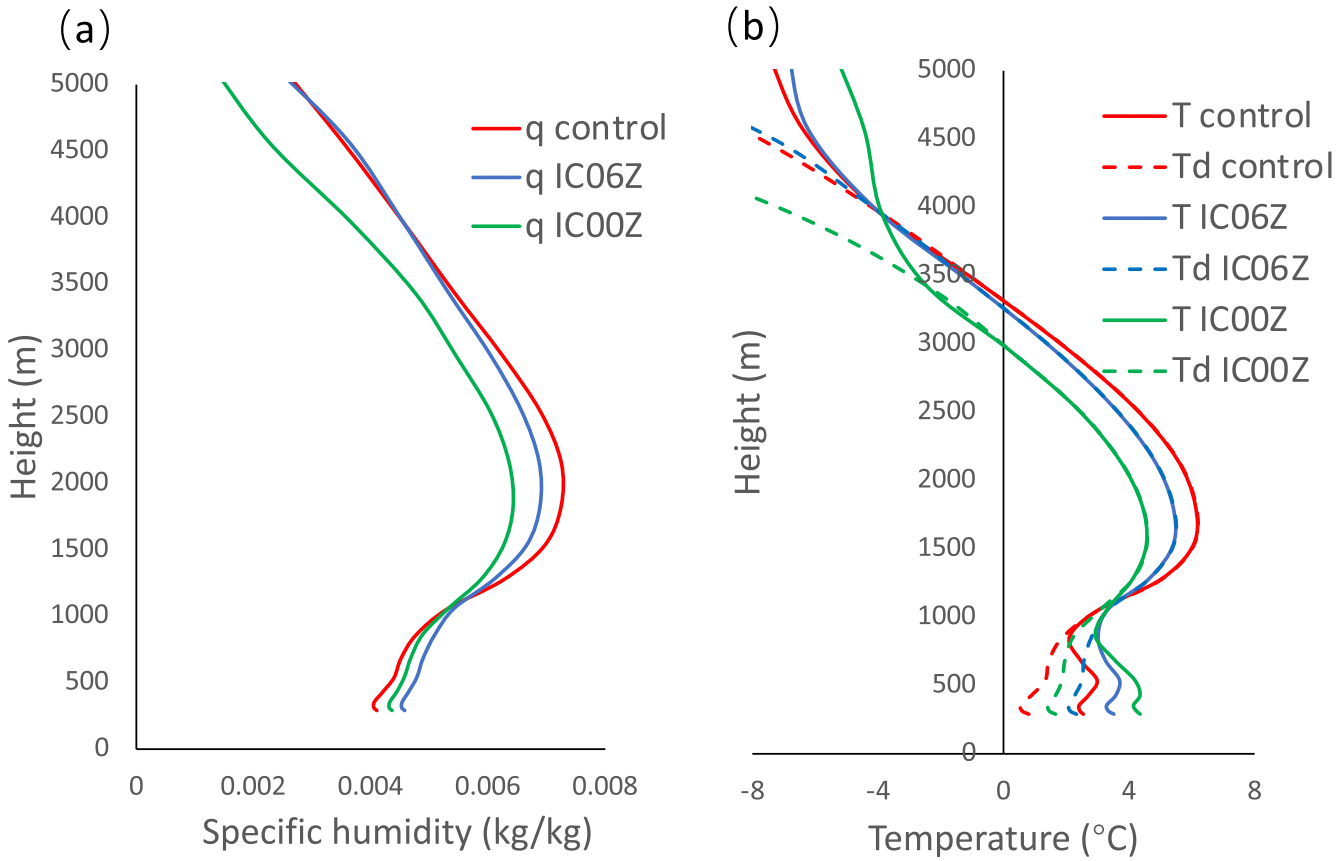

Figure 13. The vertical profile of (a) specific humidity (kg kg^{-1}) and (b) temperature (solid lines, °C), dew temperature (dashed lines, °C) in the control, IC06Z, and IC00Z runs at 19:00 UTC January 30, 2018 at the location indicated by crosses of Figure 12.

Next, we attempt to figure out why smaller precipitable water occurs in the POOR run. Figure 9 shows the comparison of temperature, dew temperature, and specific humidity in the vertical profile between the GOOD and POOR runs. At the initial time (12:00 UTC), the specific humidity above 1,000 m in the GOOD run with a maximum of 7.5 g/kg at around 2,000 m (Figure 9a) is higher than that in the POOR run with a maximum of 7.2 g/kg (Figure 9b). Such a larger specific humidity in the GOOD run is because both runs show saturation above 1,000 m (temperature equals to dew temperature) but with higher temperature (~0.3–0.7°C) in the GOOD run that can hold more moisture at the middle levels (Figures 9c and 9d). The differences in thermal variables between the two runs remain until 19:00 UTC. Therefore, thermal variables including humidity and temperature are important in the initial condition for the practical predictability of wave-convection coupled bands. In addition to comparison between the deterministic GOOD and POOR runs, we analyzed the respective compositions from the good and poor ensemble members, and found similar results as above (Figures S1 and S2 in Supporting Information S1).

By comparing GOOD and POOR runs, the thermodynamical processes (humidity and temperature) are found to be important for the predictability of wave-convection coupled bands. To further examine the sensitivity of humidity and temperature in the initial conditions and verify the key role of thermal variables in simulating the wave-convection coupled bands, we partly replace the initial condition of the POOR run with that of the GOOD run (Figure 10). When the relative humidity in the initial condition of the GOOD run is used in the POOR run (ICRH run), the simulated capability of wave features is only slightly improved (Figure 10d). Compared to the ICRH run, wave features exhibit more clearly in the ICT run where the temperature is replaced in the initial condition (Figure 10e). If both relative humidity and temperature are updated in the initial condition in the ICRHT run (Figure 10f), the wavelike banded convection is captured and pretty similar to the GOOD or control run although the other atmospheric fields (e.g., dynamic variables) in the initial condition are still from the POOR run. The slight difference of precipitable water in the

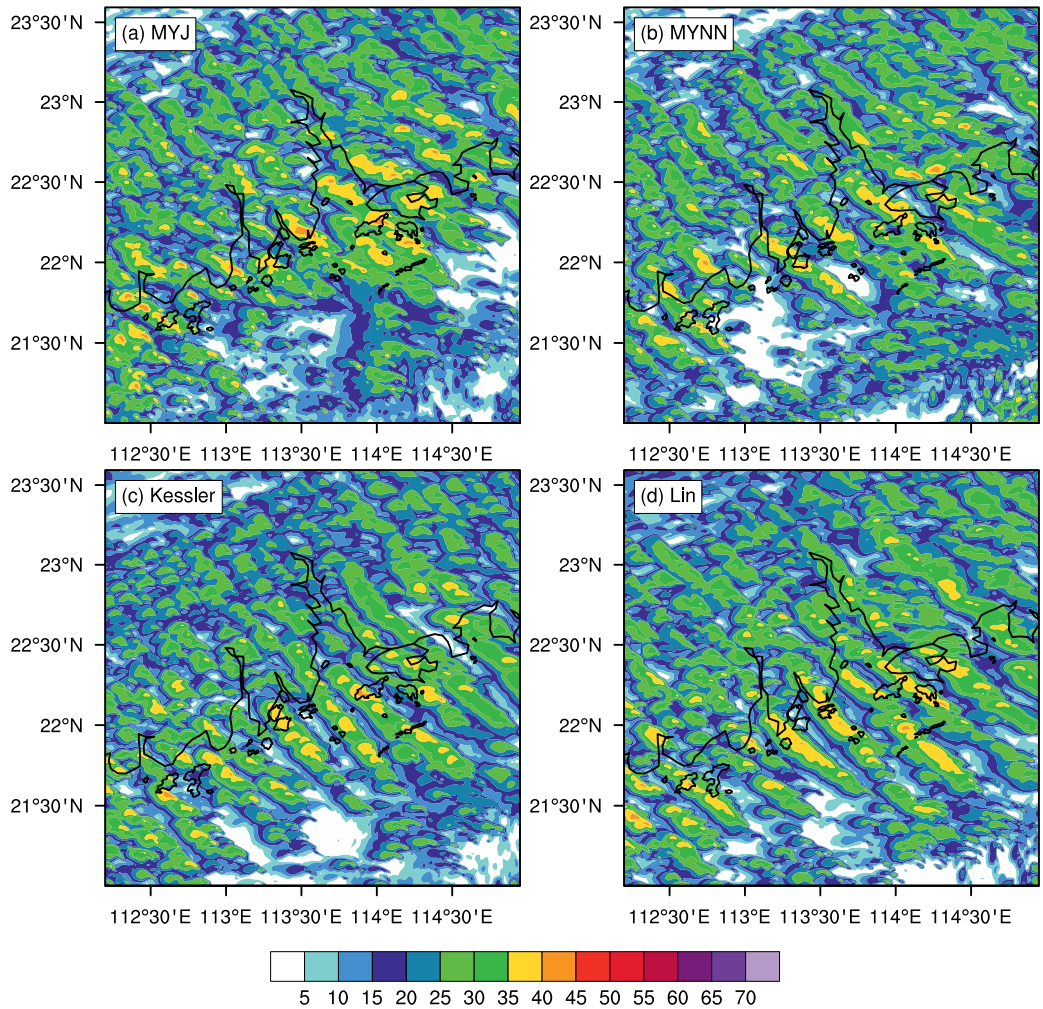

Figure 14. Simulated radar composite reflectivity at 19:00 UTC January 30, 2018 in the (a) MYJ, (b) MYNN, (c) Kessler, and (d) Lin runs.

initial condition between the GOOD run and the ICRH run (Figure 11a) greatly increases until 19:00 UTC (Figure 11b). In contrast, the differences of precipitable water in the initial condition between the GOOD run and the ICT run (Figure 11c) or the ICRHT run (Figure 11e) are smaller, which remain relatively small throughout the evolution period (Figures 11d and 11f). These sensitivity experiments above verify the importance of thermal variables in the initial condition, especially for the temperature.

4.2. Sensitivity to Initialization Times

In reality, reanalysis at a different time around the period of interest is optional to be used as an initial condition in the numerical simulations. The control simulation is initialized at 12:00 UTC January 30, 2018, whereas the IC06Z and IC00Z runs are initialized at 06:00 UTC and 00:00 UTC January 30, 2018, respectively (Figure 12). The wavelike banded convection pattern in the IC06Z run is similar to that in the control simulation except for the northeastern portion (Figure 12a) where the specific humidity and temperature within the layer of 1,000–3,500 m are smaller than those in the control run (Figure 13). However, in the IC00Z run (Figure 12b), the convection does not show a clear wavelike pattern as in the control simulation. The wave ducting in the IC06Z run is similar to that in the control simulation (Figure 7c), but the wave ducting in the IC00Z is not as clear as that in the control run (Figure 7d). In the IC00Z run, the low-level layer is less stable than that in the control simulation (Figure 7d). Meanwhile, the critical level in the IC00Z run is not completely embedded within the less-stable layer of 850–600 hPa, and the Richardson number greater

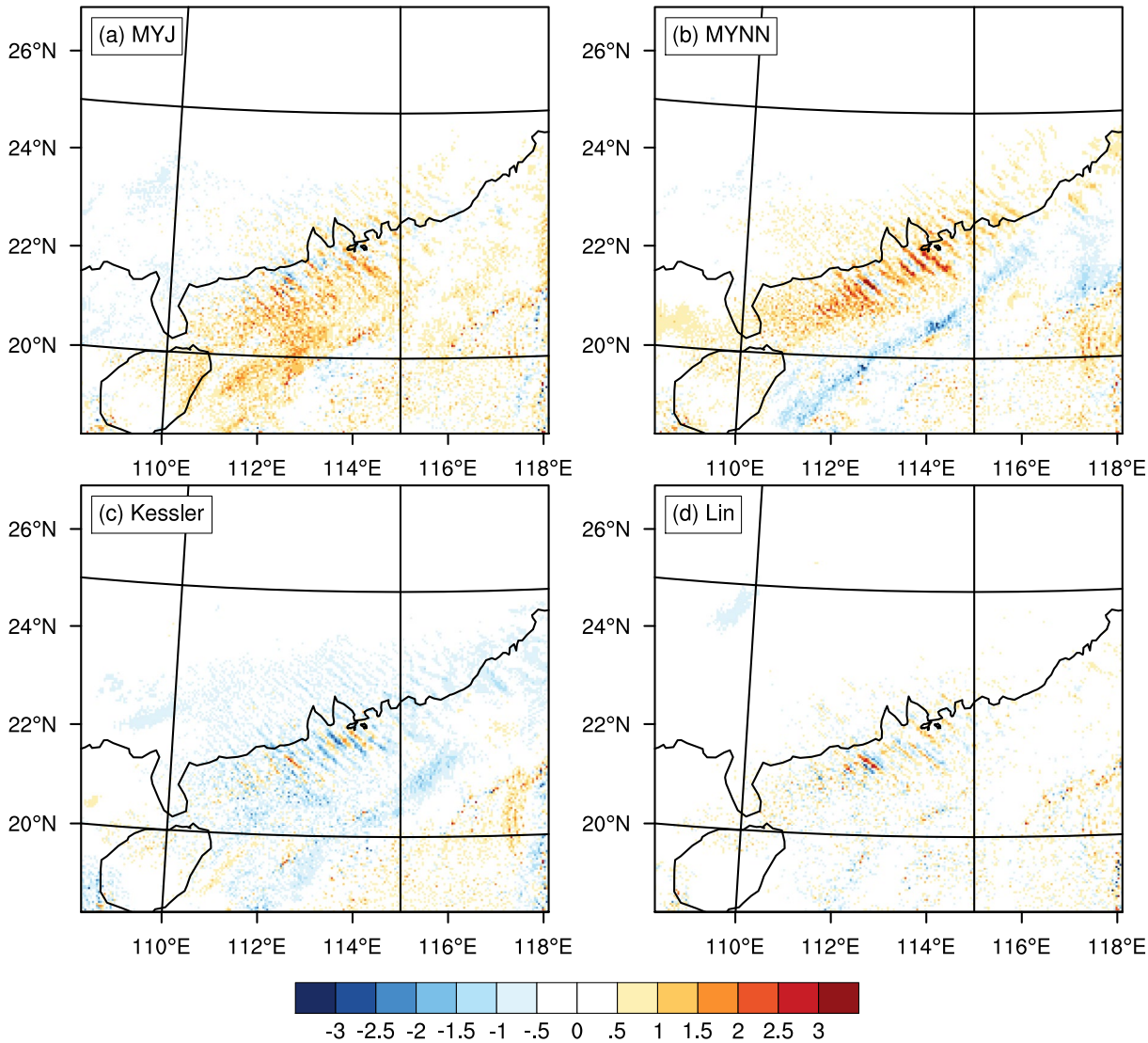

Figure 15. The difference of precipitable water (kg m^{-2}) between the GOOD run and (a) MYJ, (b) MYNN, (c) Kessler, and (d) Lin runs at 19:00 UTC January 30, 2018.

than 0.25 partly occurs around the critical level (Figure 7d). Also, the humidity and temperature above 1,000 m on land in the IC00Z run are significantly smaller than those in the control run (Figure 13). Therefore, initial conditions at different times can influence the wave ducting structure and specific humidity at middle levels and thus result in the differences in the wavelike patterns of banded convection among those simulations. The failure of the IC00Z run to capture this wavelike banded pattern also implies a limited practical forecast lead time for this event.

4.3. Sensitivity to Physical Schemes

Besides initial conditions, the options of physical schemes may affect the practical predictability. We examine the sensitivity of wavelike banded convection to physical schemes including planetary boundary layer (PBL) and microphysics parameterizations.

As for PBL schemes, Mellor-Yamada-Janjic (MYJ, Janjić, 1990) and Mellor-Yamada-Nakanishi-Niino (MYNN, Nakanishi & Niino, 2004) schemes are used to compare with the YSU scheme in the GOOD run. The two PBL schemes (MYJ and MYNN) are local-influenced and generally yield thinner PBL than nonlocal schemes (e.g., YSU scheme) (Xie et al., 2012). As shown in Figures 14a and 14b, the wavelike patterns

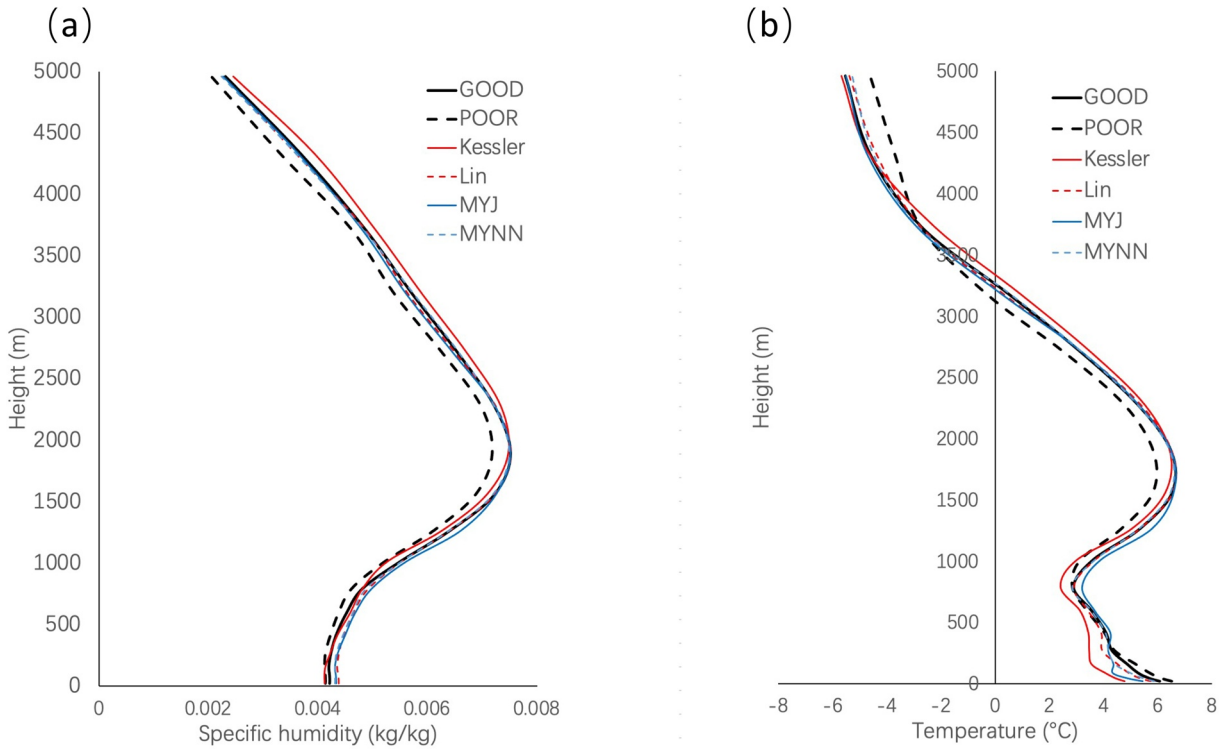

Figure 16. The vertical profile of (a) specific humidity (kg kg^{-1}) and (b) temperature (solid lines, °C) in the GOOD, POOR, Kessler, Lin, MYJ, MYNN runs at 19:00 UTC January 30, 2018 at Qingyuan.

of banded convection in the MYNN sensitivity experiment are generally similar to those in the GOOD run (Figure 10b) in their orientation (northwest-southeast), phase speed (~12 m s^{-1}) and primary wavelength (~30–40 km), while the wavelike pattern over the ocean in the MYJ run is not as clear as that in the GOOD run. Furthermore, two additional microphysics schemes (Kessler scheme and Lin et al. scheme) are used in microphysics sensitivity experiments. Figures 14c and 14d show similar wavelike patterns of banded convection as the GOOD run (Figure 10b) in their orientation, phase speed, and primary wavelength.

Generally, the wavelike patterns of banded convection are not sensitive to the physical parameterizations (e.g., PBL and microphysics) for the wavelike convection pattern in the current case, compared to the sensitivity to initial conditions. Figure 15 shows the differences of precipitable water (kg m^{-2}) between the GOOD run and those sensitivity runs on physical parameterizations. Such differences over the land (~±0.5 kg m^{-2}) are significantly smaller than the differences between the runs with different initial conditions (~±1.5 kg m^{-2} in Figure 8h). Furthermore, as shown in Figure 16, the vertical profiles of specific humidity and temperature are not sensitive among the sensitivity runs on physical parameterizations. The results further support the key role of thermal variables in simulating the wave-convection coupled bands.

5. Intrinsic Predictability

While the practical predictability for a numerical model can be largely influenced by model errors and bias, it is a common approach to adopt a perfect model assumption when studying the intrinsic predictability. To examine the intrinsic predictability limit of the wavelike banded convection, we conducted nine additional sensitivity experiments, from R1 to R9, which are initialized with linear weighted averaging all prognostic variables in the initial conditions of the GOOD and POOR runs.

Figure 17 presents the simulated reflectively for the nine simulations as well as the GOOD and POOR runs at 19:00 UTC. A trend exists from the R1 to R9 runs toward wavelike banded convection in the GOOD run. The wavelike banded convection in the R9 run is most similar to that in the GOOD run.

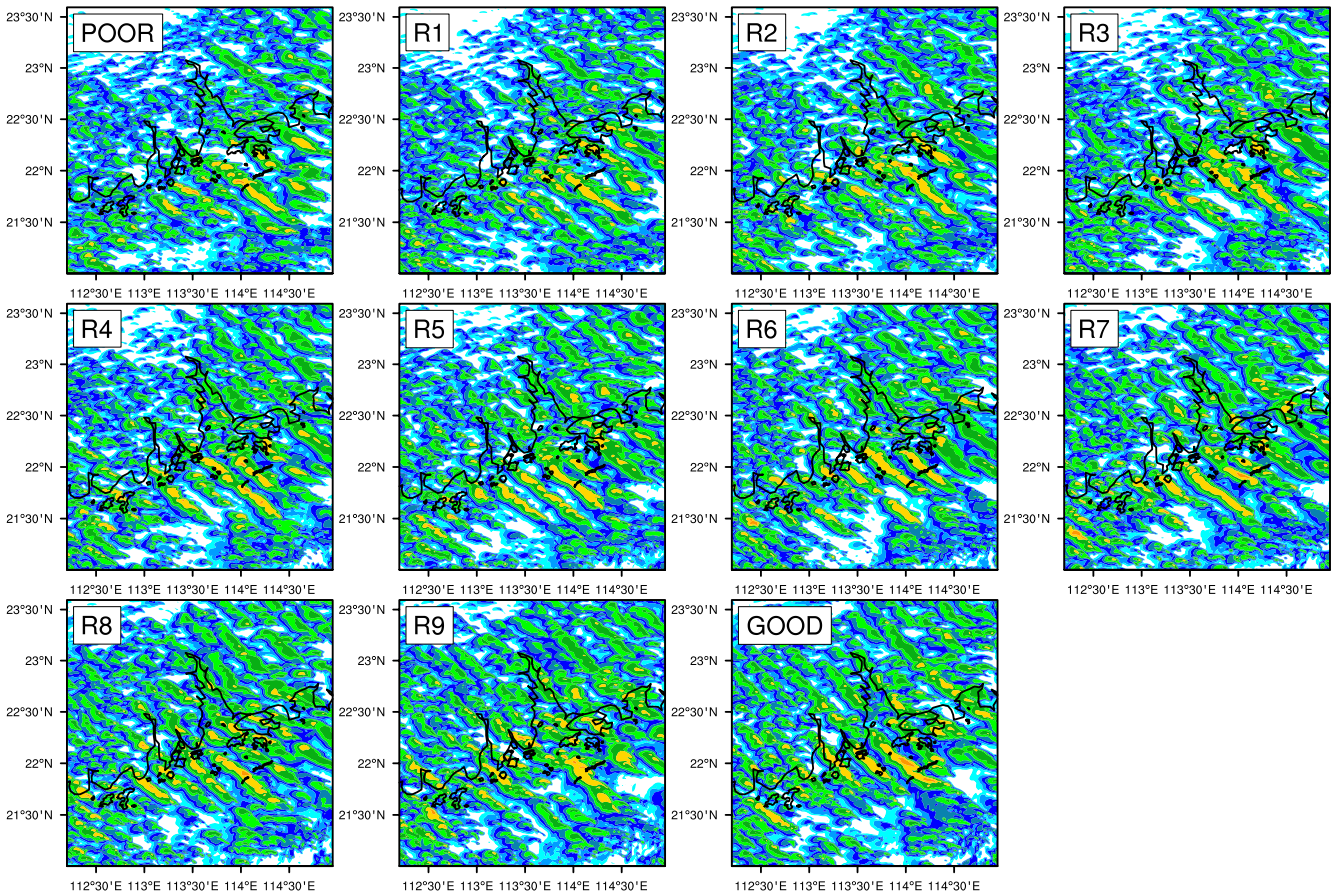

Figure 17. Simulated radar composite reflectivity at 19:00 UTC January 30, 2018 in the POOR, R1, R2, R3, R4, R5, R6, R7, R8, R9, and GOOD runs.

Wave-parallel vertical cross sections along the red line of Figure 4 of cloud water mixing ratio and vertical motion in those experiments further illustrate this gradual evolution toward the GOOD results from the R1 to R9 runs (Figure 18). All experiments show that the upward motion traveled with convective cells synergistically, which suggests the coupling of convection and gravity waves in those runs. In the R1–R5 runs, the horizontal extent and spacing of convective cells are smaller than those in the R6–R9 runs. The phase of wavelike banded convection has high uncertainties. The location of individual convective cells varies among the R1–R9 runs. Although very slight differences (only 10% errors) of initial conditions exist between the R9 and GOOD runs, the locations of individual convective cells are different between the two runs (cf. Figures 18j and 18k). Even if the errors in the initial conditions are only 1%, the location of individual convective cells are still distinct from the GOOD run (Figure S4 in Supporting Information S1). Therefore, the pattern of wave-convection coupled bands is predictable but the phase of wavelike bands is unpredictable intrinsically after a short integration time. The microphysics sensitivity experiments also imply a similar conclusion on unpredicting of the phase of wavelike bands (Figures 14c and 14d).

The error growth and predictability of the banded convection can be further examined quantitatively by the difference total energy (DTE) defined in Zhang et al. (2003, 2007) as

$$\mathrm{DTE} = \frac{1}{2}\sum\left(u'u' + v'v' + kT'T'\right)$$

where u', v', and T' are the difference in wind components and temperature between two simulations, $k = C_p T_r^{-1}$ (C_p = 1004.9 J kg^{-1} K^{-1} and T_r = 270 K, the reference temperature). $\sum$ represents the sum of vertical and horizontal grid points in the black box of Figure 4.

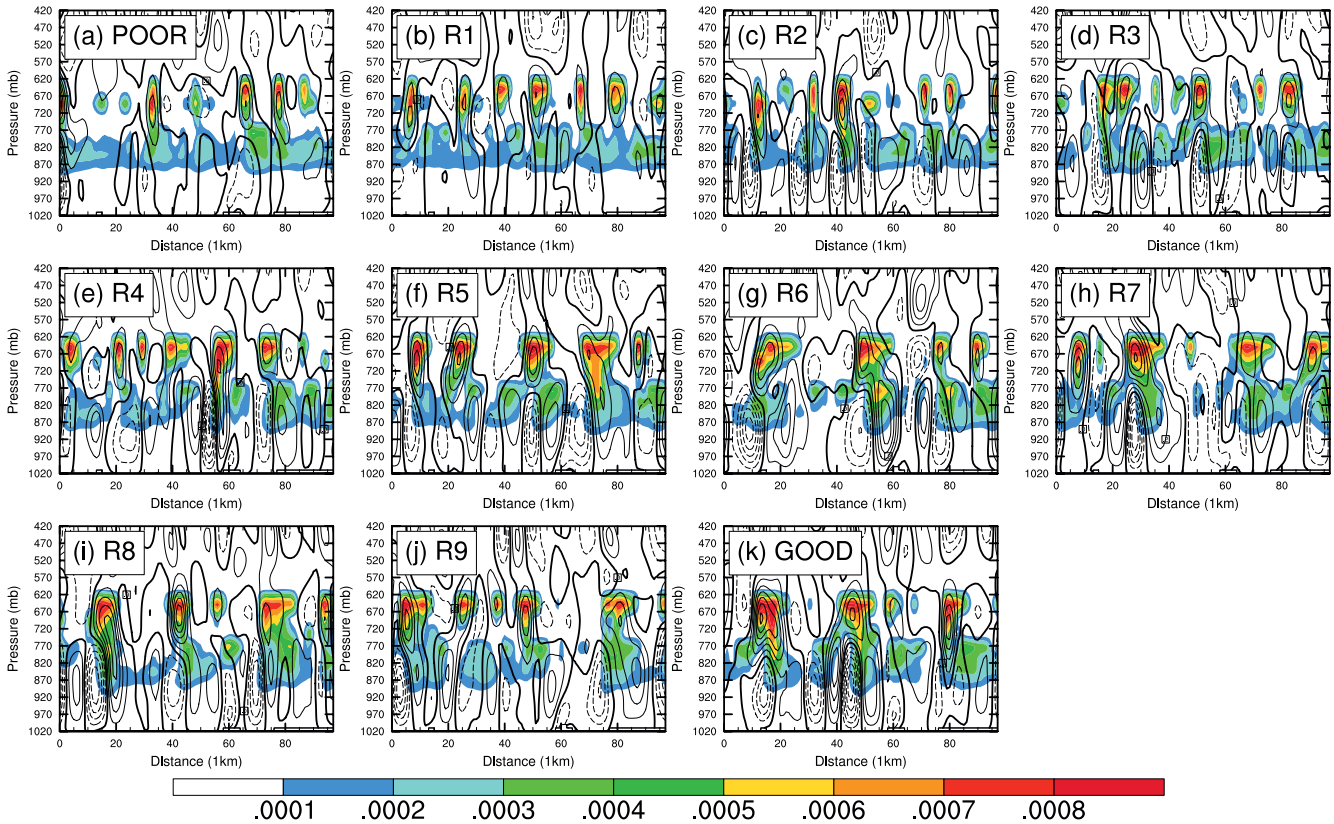

Figure 18. Wave-parallel vertical cross section of cloud water mixing ratio (shading, kg kg^{-1}) and vertical motion (contour, m s^{-1}) compositing (averaging) along the red line of Figure 4 at 19:00 UTC, January 30, 2018 in the (a) POOR, (b) R1, (c) R2, (d) R3, (e) R4, (f) R5, (g) R6, (h) R7, (i) R8, (j) R9, and (k) GOOD runs.

To identify the error growth at different scales, a two-dimensional spatial filter (Appendix in Wei et al., 2016) is applied mainly following the procedure in Zhang et al. (2007) to extract the small-scale component with horizontal wavelengths <200 km and the large-scale component with horizontal wavelengths greater than 200 km. The DTE at scales smaller than 200 km represents the errors from mesoscale gravity waves and convective instability of interest in the current case, while the DTE at scales greater than 200 km indicates the errors from large-scale background environment. Sensitivity calculations using critical numbers slightly different with 200 km are also conducted and gave very similar results (not shown here).

Figure 19a presents the temporal evolution of the DTE at the scales smaller than 200 km between GOOD and R1–R9 or POOR runs from 12:00 UTC to 21:00 UTC January 30, 2018. Small-scale small-amplitude initial errors can grow rapidly and reach saturation (DTE = ~10^6 m^2 s^{-2}) a few hours later. The smaller the initial difference is, the faster it grows, which indicates that the error growth on small scale is nonlinear. For instance, although the initial DTE between GOOD-R9 is only one hundredth of that between GOOD-POOR, the DTE between GOOD-R9 catches up quickly the DTE between GOOD-POOR 7 hr later (Figure 19a). The DTEs during 19:00–21:00 UTC are comparable to the maximum values (~10^6 m^2 s^{-2}) found in either GOOD-R9 or GOOD-POOR, indicating local error saturation at the convective scales and gravity wave scales. Such DTE behavior suggests intrinsic predictability limit at small scale (mesoscale gravity waves), which is consistent with the earlier results that the phase of wavelike bands is unpredictable intrinsically after a short integration time (~7 hr).

In contrast, the evolution of the DTE at the scales greater than 200 km shows totally different characteristics (Figure 19b). The DTE gradually increases for all indicated pairs of simulations after the model initiation, and they show similar rate of growth. Therefore, if the initial error at large scale is smaller, the error will remain smaller after a few hours. Furthermore, the errors from the large-scale background

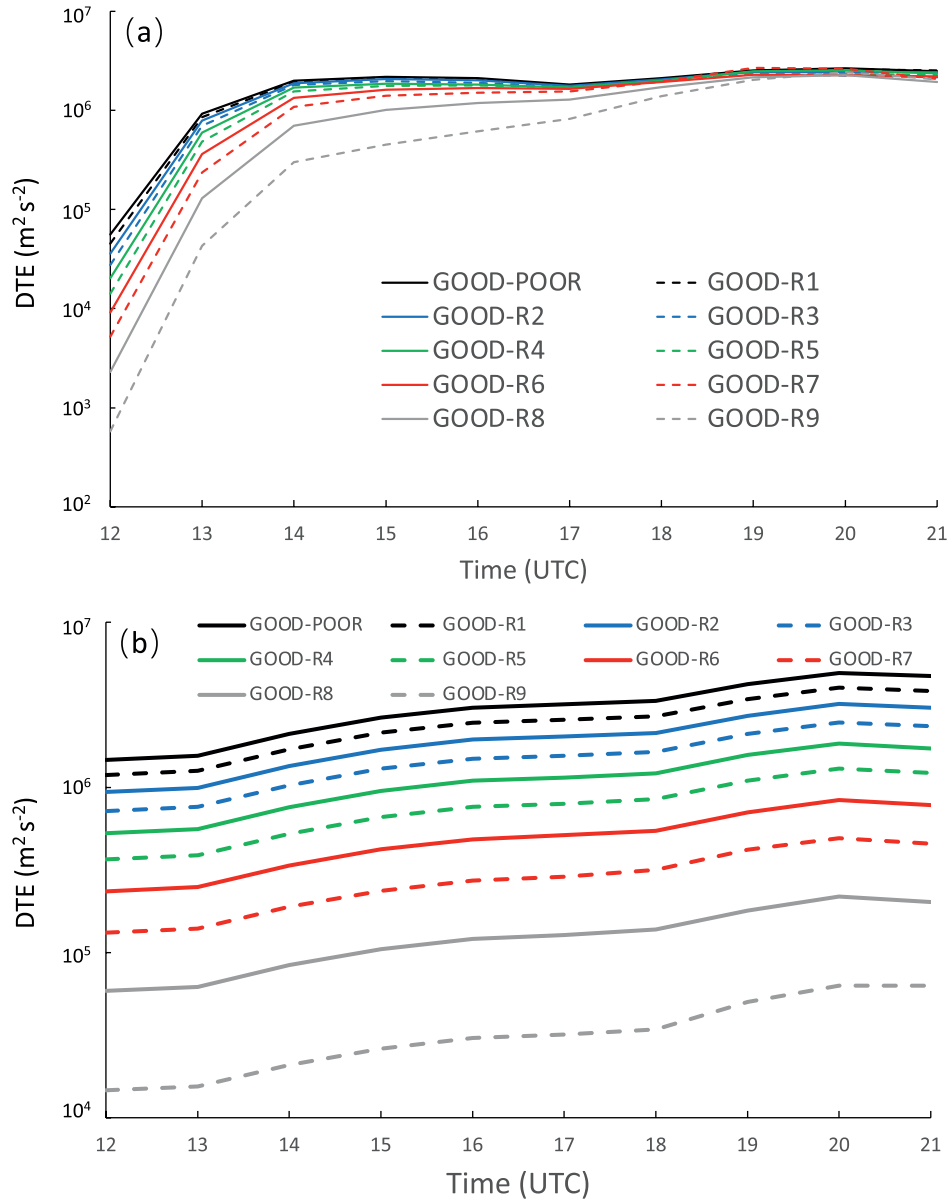

Figure 19. (a) Temporal evolution of difference total energy (DTE; $m^2\ s^{-2}$) at the scale smaller than 200 km between indicated simulations from 12:00 UTC to 21:00 UTC January 30, 2018. (b) Same as (a) except for the scale greater than 200 km.

environment, including many important wave-related features such as the wave ducting structure and the humidity field, could potentially modulate and organize the variations for the pattern of the banded convection among R1–R9 runs. A trend exists from the R1 to R9 runs toward wavelike banded convection in the GOOD run due to the gradual decrease of initial large-scale errors as well as large-scale errors a few hours later.

The gradual change of wavelike convection among the R1–R9 runs is attributed to the change of precipitable water differences (Figure 20). The precipitable water difference is significant over the land. The difference of precipitable water at 19:00 UTC between the GOOD run and R1 run is the largest among R1–R9 runs, similar to that between the GOOD and POOR runs. In contrast, the difference of precipitable water between the GOOD run and R9 run is pretty small, suggesting the R9 run is the closest to the GOOD run.

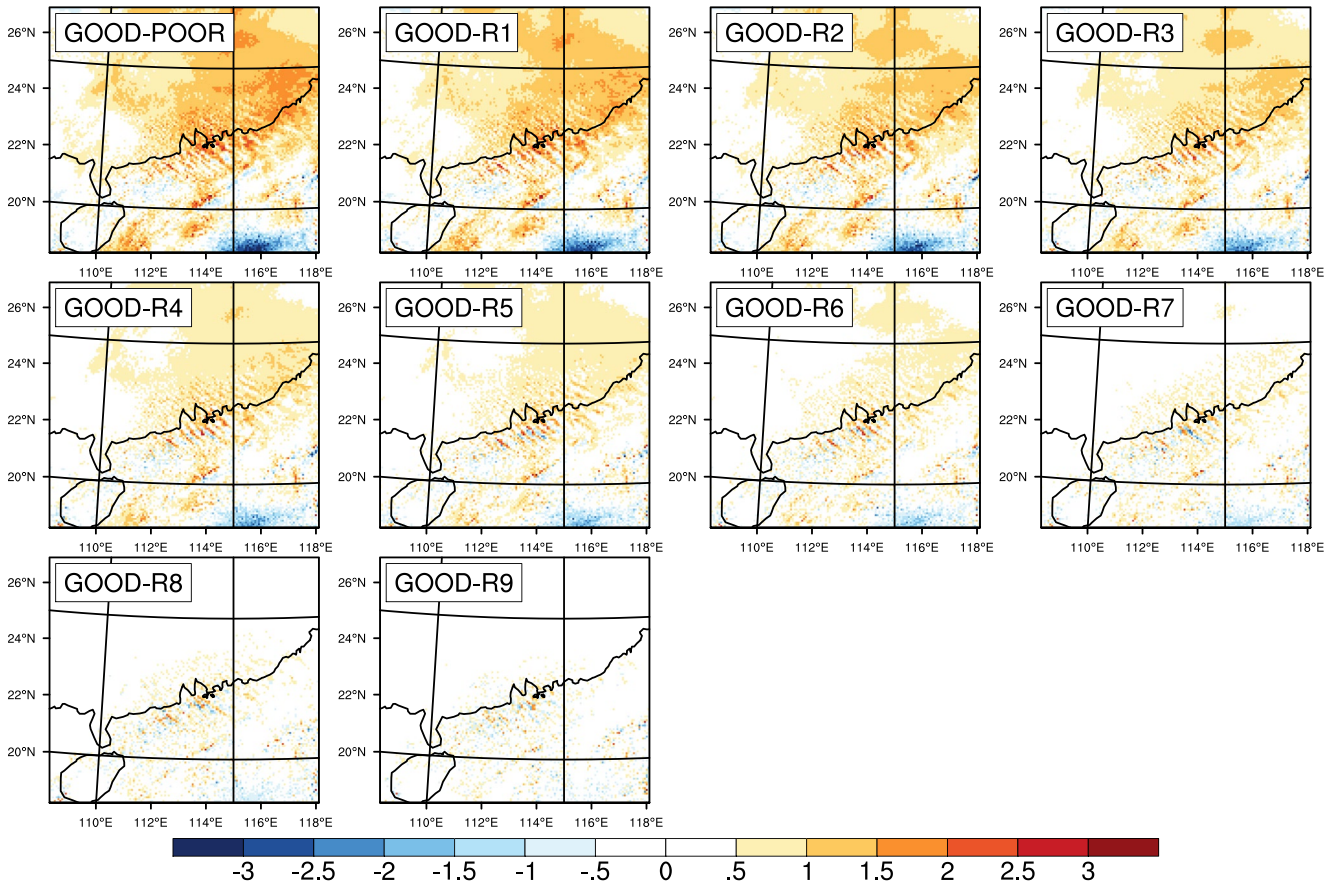

Figure 20. The difference of precipitable water (kg m^{-2}) between the GOOD run and POOR, R1, R2, R3, R4, R5, R6, R7, R8, R8, R9 runs at 19:00 UTC January 30, 2018.

6. Conclusions

In the present study, various ensemble and sensitivity numerical simulations from the Advanced Research Weather Research and Forecasting (WRF) model with a horizontal resolution of 1 km are conducted to investigate the practical and intrinsic predictability of wave-convection coupled bands near the south coast of China on January 30, 2018. DZ19 documented that a distinct wave duct existed in this event and kept the energy of gravity waves in the low levels, characterized by a thick low-level stable layer below 850 hPa capped by a less-stable reflecting layer with a critical level. Convective bands and gravity waves are collocated and interacted with each other, in which the convective bands propagate in phase with the peak updraft of gravity waves. Based on what DZ19 found, we further investigate the sensitivity of wave-convection coupled bands to initial conditions and physical schemes to the wave-convection coupled bands, as well as examine their intrinsic limit of predictability in the present study.

The 20-member ensembles initialized with GEFS can generally capture the wave-convection coupled bands near the south coast of China with similar stratification at low levels. However, wavelike patterns of convective bands over the land are more significant in some ensembles than others. Five good members and five poor members are selected into two groups, and initial conditions of each group are composited to conduct GOOD and POOR simulations. The GOOD and POOR simulations can well represent the wave behaviors in the good and poor members, respectively. Wavelike banded convection over the land in the POOR run is not as clear as that in the GOOD run. The two runs show similar propagation speed, but the horizontal wavelength is larger in the GOOD run compared to the POOR run.

To clarify the differences in wave features between the GOOD and POOR runs, we further examine environmental stratification in the GOOD and POOR runs. Both the two simulations show notable wave ducting as

found in DZ19. Significant differences of precipitable water over Guangdong are found between the GOOD and POOR runs from the initial time to the time when the wave-convection coupled bands occur. It is found that the differences in low-to-mid-level temperature and humidity (1,000–3,500 m) mainly contribute to the difference in precipitable water in the two runs. Additional sensitivity experiments on the replacement of humidity and temperature in the initial condition further verify the significance of thermal variables for the prediction of wave-convection coupled bands.

As for the practical predictability, initial conditions at different times can affect the structure of wave ducting as well as low-to-mid-level humidity and temperature, which induce varying wave-convection coupled bands among the simulations. Compared to initial conditions, physical schemes like PBL and microphysics parameterizations have a minor impact on the wave-convection coupled bands in the current case.

Additional sensitivity experiments R1–R9, which are initialized with linear weighted averaging all prognostic variables in the initial conditions of the GOOD and POOR runs, are conducted to examine the intrinsic predictability of the wave-convection coupled bands. R1 and R9 runs are closest to the POOR and GOOD runs, respectively. Overall, the wave pattern can be reproduced in those sensitivity experiments. The wavelike banded convection gets more pronounced from the R1 to R9 runs. However, the location of individual convective cells is highly uncertain although the difference in the initial condition is very slight since the error growth on small scale is nonlinear. The smaller the initial difference at small scale is, the faster it grows. Therefore, the phase of wave-convection coupled bands is unpredictable intrinsically.

The results on the predictability of wave-convection coupled bands in the present study only apply to this event. In the future, more similar cases will be studied to clarify the practical and intrinsic predictability of wave-convection coupled bands, which may vary under different atmospheric conditions.

Acknowledgments
The authors express thanks to NOAA for providing Global Ensemble Forecast System (GEFS) data (https://www.ncei.noaa.gov/products/weather-climate-models/global-ensemble-forecast) and CMA-Guangzhou Joint Research Center for Atmospheric Sciences with support from Guangdong Meteorological Bureau for providing radar and sounding data. This study was supported by the National Key Research and Development Program of China (grant 2018YFC1507402), the National Natural Science Foundation of China (grants 42122033, 41875055, 42075006, 42075005, 41861164027), Guangzhou Science and Technology Plan Projects (202002030346), the Fundamental Research Funds for the Central Universities (19lgzd08), and the Young Elite Scientists Sponsorship Program by CAST (2018QNRC001). Y. Qiang Sun is funded under Award NA18OAR4320123 from the National Oceanic and Atmospheric Administration, U.S. Department of Commerce.

References

Anthes, A., Kuo, H., Baumhefner, P., Errico, M., & Bettge, W. (1985). Predictability of mesoscale atmospheric motions. *Advances in Geophysics*, *28*(12), 159–202. https://doi.org/10.1016/S0065-2687(08)60188-0

Bei, N., & Zhang, F. (2007). Impacts of initial condition errors on mesoscale predictability of heavy precipitation along the Mei-Yu front of China. *Quarterly Journal of the Royal Meteorological Society*, *133*, 83–99. https://doi.org/10.1002/qj.20

Bosart, L. F., Bracken, W. E., & Seimon, A. (1998). A study of cyclone mesoscale structure with emphasis on a large-amplitude inertia-gravity wave. *Monthly Weather Review*, *126*(6), 1497–1527. https://doi.org/10.1175/1520-0493(1998)126<1497:ASOCMS>2.0.CO;2

Clarke, R. H. (1972). The morning glory: An atmospheric hydraulic jump. *Journal of Applied Meteorology*, *11*(2), 304–311. https://doi.org/10.1175/1520-0450(1972)011<0304:TMGAAH>2.0.CO;2

Cram, J. M., Pielke, R. A., & Cotton, W. R. (1992). Numerical simulation and analysis of a prefrontal squall line. Part II: Propagation of the squall line as an internal gravity wave. *Journal of the Atmospheric Sciences*, *49*(3), 209–225. https://doi.org/10.1175/1520-0469(1992)049<0209:NSAAOA>2.0.CO;2

Crook, N. A. (1996). Sensitivity of moist convection forced by boundary layer processes to low-level thermodynamic fields. *Monthly Weather Review*, *124*(8), 1767–1785. https://doi.org/10.1175/1520-0493(1996)124<1767:SOMCFB>2.0.CO;2

Du, Y., & Zhang, F. (2019). Banded convective activity associated with mesoscale gravity waves over southern China. *Journal of Geophysical Research: Atmospheres*, *124*, 1912–1930. https://doi.org/10.1029/2018JD029523

Gilmore, M. S., & Wicker, L. J. (1998). The influence of mid-tropospheric dryness on supercell morphology and evolution. *Monthly Weather Review*, *126*(4), 943–958. https://doi.org/10.1175/1520-0493(1998)126<0943:TIOMDO>2.0.CO;2

Hohenegger, C., & Schar, C. (2007). Atmospheric predictability at synoptic versus cloud-resolving scales. *Bulletin of the American Meteorological Society*, *88*(11), 1783–1794. https://doi.org/10.1175/BAMS-88-11-1783

Hong, S.-Y., Noh, Y., & Dudhia, J. (2006). A new vertical diffusion package with an explicit treatment of entrainment processes. *Monthly Weather Review*, *134*(9), 2318–2341. https://doi.org/10.1175/MWR3199.1

Iacono, M. J., Delamere, J. S., Mlawer, E. J., Shephard, M. W., Clough, S. A., & Collins, W. D. (2008). Radiative forcing by long-lived greenhouse gases: Calculations with the AER radiative transfer models. *Journal of Geophysical Research*, *113*, D13103. https://doi.org/10.1029/2008JD009944

Janjić, Z. I. (1990). The step-mountain coordinate: Physical package. *Monthly Weather Review*, *118*(7), 1429–1443. https://doi.org/10.1175/1520-0493(1990)118<1429:TSMCPP>2.0.CO;2

Jiménez, P. A., Dudhia, J., González-Rouco, J. F., Navarro, J., Montávez, J. P., & García-Bustamante, E. (2012). A revised scheme for the WRF surface layer formulation. *Monthly Weather Review*, *140*(3), 898–918. https://doi.org/10.1175/MWR-D-11-00056.1

Judt, F. (2018). Insights into atmospheric predictability through global convection-permitting model simulations. *Journal of the Atmospheric Sciences*, *75*(5), 1477–1497. https://doi.org/10.1175/JAS-D-17-0343.1

Kain, J. S. (2004). The Kain-Fritsch convective parameterization: An update. *Journal of Applied Meteorology*, *43*(1), 170–181. https://doi.org/10.1175/1520-0450(2004)043<0170:TKCPAU>2.0.CO;2

Koch, S. E., Golus, R. E., & Dorian, P. B. (1988). A mesoscale gravity wave event observed during CCOPE. Part II: Interactions between mesoscale convective systems and the antecedent waves. *Monthly Weather Review*, *116*(12), 2545–2569. https://doi.org/10.1175/1520-0493(1988)116<2545:AMGWEO>2.0.CO;2

Lane, T. P., & Zhang, F. (2011). Coupling between gravity waves and tropical convection at mesoscales. *Journal of the Atmospheric Sciences*, *68*(11), 2582–2598. https://doi.org/10.1175/2011JAS3577.1

Lin, Y.-L. (1987). Two-dimensional response of a stably stratified shear flow to diabatic heating. *Journal of the Atmospheric Sciences*, *44*(10), 1375–1393. https://doi.org/10.1175/1520-0469(1987)044<1375:TDROAS>2.0.CO;2

Lindzen, R. S. (1974). Wave-CISK in the tropics. *Journal of the Atmospheric Sciences*, *31*(1), 156–179. https://doi.org/10.1175/1520-0469(1974)031<0156:WCITT>2.0.CO;2

Lindzen, R. S., & Tung, K.-K. (1976). Banded convective activity and ducted gravity waves. *Monthly Weather Review*, *104*(12), 1602–1617. https://doi.org/10.1175/1520-0493(1976)104<1602:BCAADG>2.0.CO;2

Livneh, B., Restrepo, P. J., & Lettenmaier, D. P. (2011). Development of a unified land model for prediction of surface hydrology and land-atmosphere interactions. *Journal of Hydrometeorology*, *12*(6), 1299–1320. https://doi.org/10.1175/2011JHM1361.1

Lorenz, E. N. (1963). Deterministic nonperiodic flow. *Journal of the Atmospheric Sciences*, *20*(2), 130–141. https://doi.org/10.1175/1520-0469(1963)020<0130:DNF>2.0.CO;2

Lorenz, E. N. (1969). The predictability of a flow which possesses many scales of motion. *Tellus*, *21*(3), 289–307. https://doi.org/10.3402/tellusa.v21i3.10086

Lorenz, E. N. (1996). Predictability—A problem partly solved. In *Proceedings of Seminar on Predictability* (pp. 1–18). ECMWF.

Mapes, B., Tulich, S., Nasuno, T., & Satoh, M. (2008). Predictability aspects of global aqua-planet simulations with explicit convection. *Journal of the Meteorological Society of Japan*, *86A*, 175–185. https://doi.org/10.2151/jmsj.86A.175

Melhauser, C., & Zhang, F. (2012). Practical and intrinsic predictability of severe and convective weather at the mesoscales. *Journal of the Atmospheric Sciences*, *69*(11), 3350–3371. https://doi.org/10.1175/JAS-D-11-0315.1

Miller, D. A., & Sanders, F. (1980). Mesoscale conditions for the severe convection of 3 April 1974 in the east-central United States. *Journal of the Atmospheric Sciences*, *37*(5), 1041–1055. https://doi.org/10.1175/1520-0469(1980)037<1041:MCFTSC>2.0.CO;2

Nakanishi, M., & Niino, H. (2004). An improved Mellor-Yamada level-3 model with condensation physics: Its design and verification. *Boundary-Layer Meteorology*, *112*(1), 1–31. https://doi.org/10.1023/B:BOUN.0000020164.04146.98

Park, S. K. (1999). Nonlinearity and predictability of convective rainfall associated with water vapor perturbations in a numerically simulated storm. *Journal of Geophysical Research*, *104*(D24), 31575–31587. https://doi.org/10.1029/1999JD900446

Park, S. K., & Droegemeier, K. K. (2000). Sensitivity analysis of a 3D convective storm: Implications for variational data assimilation and forecast error. *Monthly Weather Review*, *128*(1), 140–159. https://doi.org/10.1175/1520-0493(2000)128<0140:SAOACS>2.0.CO;2

Powers, J. G., & Reed, R. J. (1993). Numerical simulation of the large-amplitude mesoscale gravity-wave event of 15 December 1987 in the central United States. *Monthly Weather Review*, *121*(8), 2285–2308. https://doi.org/10.1175/1520-0493(1993)121<2285:NSOTLA>2.0.CO;2

Ralph, F. M., Venkateswaran, V., & Crochet, M. (1993). Observations of a mesoscale ducted gravity wave. *Journal of the Atmospheric Sciences*, *50*(19), 3277–3291. https://doi.org/10.1175/1520-0469(1993)050<3277:OOAMDG>2.0.CO;2

Raymond, D. J. (1984). A wave-CISK model of squall lines. *Journal of the Atmospheric Sciences*, *41*(12), 1946–1958. https://doi.org/10.1175/1520-0469(1984)041<1946:AWCMOS>2.0.CO;2

Raymond, D. J. (1987). A forced gravity wave model of self-organizing convection. *Journal of the Atmospheric Sciences*, *44*(23), 3528–3543. https://doi.org/10.1175/1520-0469(1987)044<3528:AFGWMO>2.0.CO;2

Ruppert, J. H., Jr., & Bosart, L. F. (2014). A case study of the interaction of a mesoscale gravity wave with a mesoscale convective system. *Monthly Weather Review*, *142*(4), 1403–1429. https://doi.org/10.1175/MWR-D-13-00274.1

Skamarock, W. C., Klemp, J. B., Dudhia, J., Gill, D. O., Barker, D., Duda, M. G., et al. (2008). *A description of the Advanced Research WRF version 3* (p. 113). NCAR Tech. Note NCAR/TN-4751STR. https://doi.org/10.5065/D68S4MVH

Sun, Y. Q., & Zhang, F. (2016). Intrinsic versus practical limits of atmospheric predictability and the significance of the butterfly effect. *Journal of the Atmospheric Sciences*, *73*(3), 1419–1438. https://doi.org/10.1175/JAS-D-15-0142.1

Tan, Z.-M., Zhang, F., Rotunno, R., & Snyder, C. (2004). Mesoscale predictability of moist baroclinic waves: Experiments with parameterized convection. *Journal of the Atmospheric Sciences*, *61*(14), 1794–1804. https://doi.org/10.1175/1520-0469(2004)061<1794:MPOMBW>2.0.CO;2

Thompson, G., Field, P. R., Rasmussen, R. M., & Hall, W. D. (2008). Explicit forecasts of winter precipitation using an improved bulk microphysics scheme. Part II: Implementation of a new snow parameterization. *Monthly Weather Review*, *136*(12), 5095–5115. https://doi.org/10.1175/2008MWR2387.1

Thompson, P. D. (1957). Uncertainty of initial state as a factor in the predictability of large scale atmospheric flow patterns. *Tellus*, *9*(3), 275–295. https://doi.org/10.3402/tellusa.v9i3.9111

Toth, Z., & Kalnay, E. (1993). Ensemble forecasting at NMC: The generation of perturbations. *Bulletin of the American Meteorological Society*, *74*(12), 2317–2330. https://doi.org/10.1175/1520-0477(1993)074<2317:EFANTG>2.0.CO;2

Tribbia, J. J., & Baumhefner, D. P. (2004). Scale interactions and atmospheric predictability: An updated perspective. *Monthly Weather Review*, *132*(3), 703–713. https://doi.org/10.1175/1520-0493(2004)132<0703:SIAAPA>2.0.CO;2

Uccellini, L. W., & Koch, S. E. (1987). The synoptic setting and possible energy sources for mesoscale wave disturbances. *Monthly Weather Review*, *115*(3), 721–729. https://doi.org/10.1175/1520-0493(1987)115<0721:TSSAPE>2.0.CO;2

Wei, J., Zhang, F., & Richter, J. H. (2016). An analysis of gravity wave spectral characteristics in moist baroclinic jet-front systems. *Journal of the Atmospheric Sciences*, *73*(8), 3133–3155. https://doi.org/10.1175/JAS-D-15-0316.1

Wheeler, M., & Kiladis, G. N. (1999). Convectively coupled equatorial waves: Analysis of clouds and temperature in the wavenumber-frequency domain. *Journal of the Atmospheric Sciences*, *56*(3), 374–399. https://doi.org/10.1175/1520-0469(1999)056<0374:CCEWAO>2.0.CO;2

Xie, B., Fung, J. C. H., Chan, A., & Lau, A. (2012). Evaluation of nonlocal and local planetary boundary layer schemes in the WRF model. *Journal of Geophysical Research*, *117*, D12103. https://doi.org/10.1029/2011JD017080

Ying, Y., & Zhang, F. (2017). Practical and intrinsic predictability of multi-scale weather and convectively coupled equatorial waves during the active phase of an MJO. *Journal of the Atmospheric Sciences*, *74*(11), 3771–3785. https://doi.org/10.1175/JAS-D-17-0157.1

Zhang, F., Bei, N., Rotunno, R., Snyder, C., & Epifanio, C. C. (2007). Mesoscale predictability of moist baroclinic waves: Convection-permitting experiments and multistage error growth dynamics. *Journal of the Atmospheric Sciences*, *64*(10), 3579–3594. https://doi.org/10.1175/JAS4028.1

Zhang, F., Davis, C. A., Kaplan, M. L., & Koch, S. E. (2001). Wavelet analysis and the governing dynamics of a large-amplitude mesoscale gravity-wave event along the East Coast of the United States. *Quarterly Journal of the Royal Meteorological Society*, *127*, 2209–2245. https://doi.org/10.1002/qj.49712757702

Zhang, F., & Koch, S. E. (2000). Numerical simulations of a gravity wave event over CCOPE. Part II: Waves generated by an orographic density current. *Monthly Weather Review*, *128*(8), 2777–2796. https://doi.org/10.1175/1520-0493(2000)128<2777:NSOAGW>2.0.CO;2

Zhang, F., Snyder, C., & Rotunno, R. (2003). Effects of moist convection on mesoscale predictability. *Journal of the Atmospheric Sciences*, *60*(9), 1173–1185. https://doi.org/10.1175/1520-0469(2003)060<1173:EOMCOM>2.0.CO;2

Zhang, F., Sun, Y. Q., Magnusson, L., Buizza, R., Lin, S.-J., Chen, J.-H., & Emanuel, K. (2019). What is the predictability limit of midlatitude weather? *Journal of the Atmospheric Sciences*, *76*(4), 1077–1091. https://doi.org/10.1175/JAS-D-18-0269.1

Zhang, Y., Zhang, F., Stensrud, D. J., & Meng, Z. (2016). Intrinsic predictability of the 20 May 2013 tornadic thunderstorm event in Oklahoma at storm scales. *Monthly Weather Review*, *144*(4), 1273–1298. https://doi.org/10.1175/MWR-D-15-0105.1